

# Cosmological imprints in the filament with DisPerSE

Ziyong Wu<sup>1,2</sup>, Yu Luo<sup>5,1\*</sup>, Wei Wang<sup>1,2</sup>, Xi Kang<sup>3,4,1†</sup>, Renyue Cen<sup>4,3</sup>

<sup>1</sup>Purple Mountain Observatory, Chinese Academy of Sciences, 10 Yuanhua Road, Nanjing 210033, China

<sup>2</sup>School of Astronomy and Space Sciences, University of Science and Technology of China, Hefei 230026, China,

<sup>3</sup>Institute for Astronomy, The school of Physics, Zhejiang University, Hangzhou 310037, China

<sup>4</sup>Center for Cosmology and Computational Astrophysics, Zhejiang University, Hangzhou 310027, China

<sup>5</sup>Department of Physics, School of Physics and Electronics, Hunan Normal University, Changsha 410081, China

Accepted XXX. Received YYY; in original form ZZZ

## ABSTRACT

In the regime of cosmology and large-scale structure formation, filaments are vital components of the cosmic web. This study employs statistical methods to examine the formation, evolution, and cosmological constraints of filaments identified by DisPerSe. We run large-sample of N-body simulations to study the filament length and mass functions and their evolution. In general, the filament length function can be fitted by a power law with both the normalization and power index dependent on redshift and cosmological parameters. It is discovered that filament properties are influenced by various cosmological parameters, with  $\sigma_8$  and  $n_s$  exhibiting slightly stronger dependence than  $\Omega_m$ . We also uncover a three-stage filament formation process from  $z \sim 3$  to  $z \sim 1$ : rapid formation of long and short filaments from  $z \sim 3$  to  $z \sim 2$ , persistence of long filaments from  $z \sim 2$  to  $z \sim 1$ , followed by fragmentation and increased prevalence of shorter filaments below  $z \sim 1$ . Additionally, both large and small-scale perturbations in power spectrum influence filament growth, with a characteristic scale around  $k \sim 0.265$ , wherein changes in matter fluctuations larger than this scale result in the formation of long filaments, while changes smaller than this scale have the opposite effect. These insights enhance our understanding of filament evolution and their cosmological relevance and also highlight their potential cosmological applications in observations.

**Key words:** Cosmology: cosmological parameters – large-scale structure of universe; Methods: statistical

## CONTENTS

- 1 Introduction
- 2 Method
  - 2.1 Dataset
  - 2.2 Filament pipeline
- 3 Results
  - 3.1 Cosmic variance
  - 3.2 Cosmological parameters
  - 3.3 Redshift evolution
  - 3.4 Correlation function
  - 3.5 Initial condition
- 4 Conclusion
- A Robustness

## 1 INTRODUCTION

The structure of the Universe on a large scale is in a web-like pattern referred to as the cosmic web (Bond et al. 1996) composed of clusters, filaments, walls, and voids. It is a colossal system of dark matter and baryon that emerged due to gravity’s influence from the anisotropic collapse of initial density field fluctuations (Zel’dovich 1970). One of the principal challenges in observational and theoretical cosmology is to comprehend the physical properties and evolution of the different structures of the cosmic web.

Numerical simulations demonstrate that the cosmic web is characterized by the formation of nodes in dense regions, interconnected by filaments and sheets, while most regions are dominated by voids with incredibly low density. Filament plays an import role in large scale structures. Although galaxy clusters are easily detected and characterised in the large-scale structure and galaxy formation, it is predicted that filamentary structures contain the largest fraction of baryon (Aragón-Calvo et al. 2010a; Cen & Ostriker 2006; Cautun et al. 2014). With the advent of wide-area spectroscopic redshift surveys, filaments can be detected by surveys such as the Two-Degree Field Galaxy Redshift Survey (2dFGRS, Colless et al. (2003)), the Sloan Digital Sky Survey (SDSS, Gunn et al. (2006)), the Galaxy And Mass Assembly survey (GAMA, Driver et al. (2011)), the Vimos Public Extragalactic Redshift Survey (VIPERS, Scodreggio et al. (2018)), two micron all sky survey (2MASS, Gunn et al. (2006)), and the COSMOS survey (Laigle et al. 2018). Therefore, filaments

\* luoyupmo@gmail.com

† kangxi@zju.edu.cn

could in principle play a pivotal role as cosmological probes, making it imperative to study their properties, evolution, and dependence on cosmological parameters and initial condition.

Considerable efforts were made towards developing and researching methods to detect and identify the filamentary structures, with a lot of work accomplished in this field. Libeskind et al. (2018) analysed the filaments detected by various methods and classified them into six groups based on their main characteristics: graph and percolation techniques (e.g. MST, Alpaslan et al. (2014), T-Rex method, Bonnaire et al. (2020)), stochastic methods (e.g. BISOUS model, Tempel et al. (2016)), geometric Hessian-based methods (e.g. MMF, Aragón-Calvo et al. (2007), SHMAFF, Bond et al. (2010)), scalespace Hessian-based methods (e.g. NEXUS, Cautun et al. (2013)), topological methods (e.g. DisPerSE, Sousbie (2011), SpineWeb, Aragón-Calvo et al. (2010b)), phase-space methods (e.g. ORIGAMI, Falck et al. (2012)). Meanwhile, as filaments are seen as the bridge of clusters which aggregate matter to clusters (Pogosyan et al. 2009), the primary focus of filament research lies in investigating the statistical properties of galaxies in the vicinity of cosmic filaments as well as exploring the interplay between filamentary environments and the properties of galaxies within them using different surveys such as GAMA (Kraljic et al. 2018), COSMOS (Laigle et al. 2018), VIPERS (Malavasi et al. 2017), SDSS (Chen et al. 2017; Kuutma et al. 2017; Tanimura et al. 2019; de Graaff et al. 2019), which have found significant separations of galaxy masses and types, in which massive or quench galaxies are closer to filament galaxies than smaller or active ones, underlining the fact that filaments play a role in shaping galaxy properties. While observation is hard either in SZ or in X-rays for the low density and low temperature, simulations such as HORIZON-AGN (Kraljic et al. 2019), ENZO (Gheller & Vazza 2019), IllustrisTNG (Martizzi et al. 2019) also have been applied to study gas around cosmic filaments. The implication from these studies is that the evolution of large-scale structures over cosmic time affects the potential wells of dark matter, ultimately influencing the formation of host galaxies. As a result, the information contained in the filaments can serve as a valuable tool for measuring large-scale structures and testing cosmological theories. Wilding et al. (2021) utilizes the persistent points belonging to filaments to investigate their property, specifically the density range of filaments. Meanwhile, other researchers concentrate on analyzing the length, width, and shape of filaments, including their connections. Consistent analysis of observational data has revealed a wide range of filament lengths, ranging from short structures with lengths of approximately  $5h^{-1}Mpc$  to exceedingly long objects that extend beyond  $100h^{-1}Mpc$  (Bharadwaj et al. 2004; Pimblet et al. 2004; Pandey et al. 2011; Tempel et al. 2014). Smith et al. (2012) and Pimblet et al. (2004) have also observed that short filaments tend to be straight, while very extended objects, although they are prominent in the distribution of haloes and galaxies, are rare and represent only a small fraction of the filament population (González & Padilla 2010; Tempel et al. 2014). Galárraga-Espinosa et al. (2020) discovered that filament density varies with filament length, with longer filaments being less dense than those in different simulations. Choi et al. (2010), on the other hand, found that the distribution of dark matter filament width evolves from  $z \sim 3$  to  $z \sim 0$ , with the distribution broadening and peaking at smaller widths as the universe expands. Meanwhile, the research of Cautun et al. (2014) investigated the relationship between filament length and properties such as mass, diameter, and shape across a range of redshift, spanning from  $z = 2$  to  $z = 0$ . They discovered that individual object mass and length are related through the formula  $M \propto L^{2.2}$ , and the most prominent filaments have already formed since at least  $z = 2$ , with

little change in shape and size. While many properties of filaments have been studied, little is currently known about the information filaments carry about the underlying cosmological model or how initial conditions affect filament formation.

Over the past few years, numerous studies have explored various research directions to combat degeneracies and surpass simple power spectrum analyses. These directions include incorporating information from higher-order statistics (Hahn et al. 2020; Hahn & Villaescusa-Navarro 2021; Gualdi et al. 2021; Philcox et al. 2022), velocities (Mueller et al. 2015; Kuruvilla & Aghanim 2021; Kuruvilla 2022), marked two point correlation function and power spectrum (Massara et al. 2021, 2022; Philcox et al. 2021; Yang et al. 2020; Xiao et al. 2022; Fang et al. 2019), tomographic Alcock-Paczynski (AP) (Li et al. 2014, 2015, 2016, 2018; Luo et al. 2019), wavelet scattering transform (Allys et al. 2020; Cheng et al. 2020; Cheng & Ménard 2021; Valogiannis & Dvorkin 2022b,a; Eickenberg et al. 2022; Wang & He 2022; Wang et al. 2022), split densities (Uhlemann et al. 2020; Paillas et al. 2021), partial or total cosmological environments with two point correlation function or power spectrum (Yang et al. 2005; Li et al. 2012; Cai et al. 2015; Hamaus et al. 2015; Pisani et al. 2015; Hamaus et al. 2016, 2017; Verza et al. 2019; Kreisch et al. 2022; Bayer et al. 2021; Woodfinden et al. 2022; Bonnaire et al. 2022a,b; Paillas et al. 2023), cluster density function (Vikhlinin et al. 2009; Mantz et al. 2010; Hasselfield et al. 2013; Planck Collaboration et al. 2016; Bocquet et al. 2019; Costanzi et al. 2019, 2021). These implications suggest that we can identify additional tracers to extract information about cosmology and the large scale structure of the universe. Filaments provide a promising avenue for studying the universe, and their properties can be used to constrain cosmological parameters and examine the initial conditions of the universe. In this paper, we focus specifically on one property of filaments - their length - to investigate how cosmology and initial conditions affect filament formation. We explore the potential of filament length as a new tool for cosmological statistics in various ways. As we can detect more galaxies even in more precise accuracy in the sky surveys such as Dark Energy Spectroscopic Instrument (DESI Collaboration et al. 2016), Euclid (Laureijs et al. 2011), the Nancy Grace Roman space telescope (Spergel et al. 2015) and the Chinese Space Station Telescope (CSST) to build the filaments in large scale structure, our methods may have a valuable and promising application to constrain the cosmology parameters. Additionally, we present a simple test aimed at understanding how initial fluctuations influence filament formation, which can help uncover the hidden cosmological information embedded in the cosmic web.

The layout of this paper is as follows. In Sect. 2, we introduce the simulation data used in this study as well as the filament finder methods. Detail analysis of the filament length function is presented in Sect. 3, and finally the conclusion and discussion are present in Sect. 4.

## 2 METHOD

### 2.1 Dataset

We utilized a data set that was simulated using the COMoving Lagrangian Acceleration (COLA) code. COLA calculates the movement of dark matter particles in a comoving frame, following the trajectories forecasted by Lagrangian Perturbation Theory (LPT), enabling it to accurately handle small-scale structures while preserving accuracy on large scales. Despite being hundreds of times faster than N-body simulations, it maintains high precision from very large

to highly non-linear scales. To explore various aspects of filament length statistics and evaluate the impact of numerical noise on analysis results and test robustness, we utilized *cola* to generate 1160 sets of pure dark matter cosmological simulations with different parameters. These simulations can be broadly categorized as follows:

1) To investigate the impact of varying particle numbers on filament searches and statistics, we conducted three sets of simulations, each with a different number of particles, resulting in a total of 15 simulations. The cosmological parameters of Planck15, specifically  $\Omega_m = 0.308$ ,  $\Omega_b = 0.05$ ,  $\sigma_8 = 0.83$ ,  $n_s = 0.968$ , and  $H_0 = 67.8 \text{ km s}^{-1} \text{ Mpc}^{-1}$ , were utilized to generate a box of size  $512^3 (\text{Mpc}/h)^3$ . The three sets of simulations consisted of  $128^3$ ,  $256^3$ , and  $512^3$  particles, with each set including five simulations generated with different random seeds.

2)  $\Lambda$ CDM simulation. 40 standard cosmological simulations. We generated 40 standard cosmological simulations, where each simulation box had a size of  $512^3 (\text{Mpc}/h)^3$  and  $256^3$  particles. To investigate the sensitivity of filament length functions to cosmology, we tested the magnitude of cosmic variance. Additionally, we used the 40 standard cosmological simulations to solve the covariance matrix and determine the sensitivity of filament length functions to cosmology.

3) C1 simulation. 30 sets of cosmological simulations with different cosmology. To investigate changes in filament statistics across various cosmological parameters and to determine whether filaments can be used to restrict cosmology, we generated 30 sets of cosmological simulations. Each set consisted of 10 simulations, produced by varying one of the three cosmological parameters ( $\Omega_m$ ,  $\sigma_8$ ,  $n_s$ ) while keeping the other two constant. We used a box size of  $512^3 (\text{Mpc}/h)^3$  and  $256^3$  particles per simulation, and generated five different simulations per set using different random seeds.

4) I1 simulation. Simulations of 80 different initial power spectra. In order to study how changes in the evolution of filament formation are affected by fluctuations in the initial conditions, and to decouple the effects of fluctuations of different scales on filament formation, we varied the initial fluctuations at 10 different scales. Each set of initial fluctuations at a specific scale contained 8 different fluctuation amplitudes, for a total of 80 sets. For each set of fluctuations, we generated 3 simulations with different random seeds, with a box size of  $512^3 (\text{Mpc}/h)^3$  and  $256^3$  particles.

5) The Quijote dataset. The Quijote dataset utilizes Gadget-3 to conduct a comprehensive range of simulations across various cosmological parameters. With access to this dataset, we can accurately investigate the behavior of filament statistics and their dependence on different cosmological parameters.

6) SC1 and SC2 simulation. Simulations similar to C1 and I1 but with a box size of  $300^3 (\text{Mpc}/h)^3$  and  $512^3$  particles.

6) P1 and P2 simulation. Simulations with nearly the same setting as the  $\Lambda$ CDM simulation, but with  $128^3$  and  $512^3$  particles to test the robustness of our analysis.

By using *cola*, we can readily acquire an extensive set of cosmological simulations, enabling us to extract significant physical insights and cosmic initial conditions from this intricate, nonlinear cosmological system. This process enhances our comprehension of cosmology and facilitates the development of more effective methods for observations to constrain cosmology.

## 2.2 Filament pipeline

After obtaining a cosmological simulation, we can use the CIC method to generate density fields for specific snapshots. These den-

sity fields allow us to easily identify the components of the cosmic web at each redshift snapshot using the DisPerSE method. The advantage of using density fields is that it reduces filament misidentification caused by random noise. Furthermore, the similarity between the density field of matter and dark matter halo in high-precision simulations enables our research results to be applicable to actual observations. To enhance the realism and smoothness of the identified structures, we perform  $2 \text{ Mpc}/h$  Gaussian smoothing on the density field. This smoothing largely eliminates noises in the density field below a mass scale of  $10^{12} M_\odot h^{-1}$  and filaments of length of approximately below  $1 \text{ Mpc}/h$ .

The DisPerSE method incorporates an  $N_\sigma$  parameter that characterizes topological persistence, aiding in the identification of robust components of the filamentary network in comparison to a discrete random Poisson distribution. A higher  $N_\sigma$  value facilitates the exclusion of less significant critical points, thereby preserving only the most topologically robust features. In our study, we adopt  $N_\sigma = 3$  as it has been widely used in previous studies. The DisPerSE method identifies the critical points of the density field using the Morse method, where  $S = 4, 3, 2, 1$  corresponds to bifurcation, node, saddle, and void, respectively. The saddle connects two nodes to form a filament (Kraljic et al. 2019), and bifurcation is where multiple filaments intersect, which is considered unresolved clusters and the location where superclusters exist. Building upon the cluster-filament-cluster configuration proposed by (Bond et al. 1996) and taking into account the physical considerations discussed earlier, we define a complete filament as a high-density line connecting two nodes or bifurcations, or linking a cluster and bifurcation.

DisPerSE segments the identified filaments into multiple parts, which are then reconnected to form a complete filament based on our definition. Fig. 1 illustrates the critical points and segments of filaments obtained by DisPerSE. Colors are employed to differentiate between individual filaments. Finally, we calculate the length of all complete filaments to obtain the filament length function. This complete pipeline, starting from the initial power spectrum and given different cosmological parameters, allows us to obtain the statistics of filament lengths. The following steps are involved in the pipeline:

1) After inputting the initial power spectrum and cosmological parameters, use COLA to obtain snapshots at different redshifts.

2) Apply the CIC method to the snapshot obtained at a certain redshift to obtain a smoothed density field. Use the DisPerSE method to obtain the various components of filaments.

3) Construct a complete list of filaments according to their definition.

4) Obtain various statistical measures for each filament.

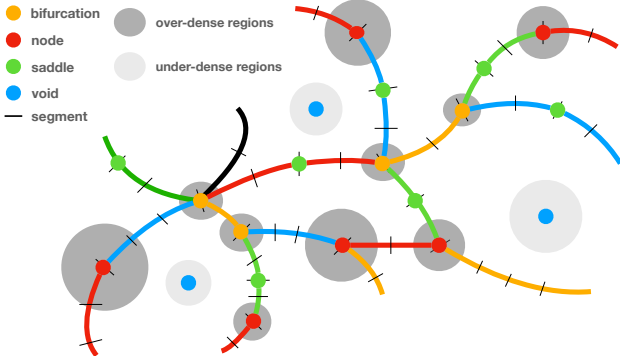
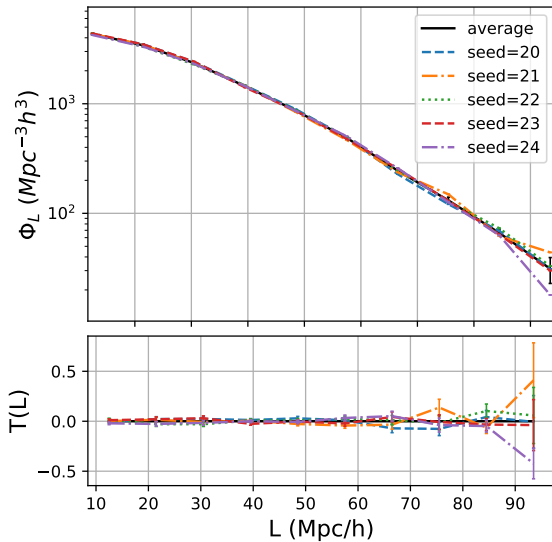
Theoretically, we can utilize this pipeline to examine numerous filament statistics, and the pipeline indicates that the statistics are solely dictated by the initial power spectrum and cosmological parameters. Nonetheless, it's crucial to highlight that this pipeline comprises several modifiable parameters, such as the box size, particle count, CIC grid size, and density field smoothing scale. These parameters significantly impact the final filament list, and their numerical effects could potentially influence the statistical findings. Thus, we will comprehensively analyze them in the subsequent discussion.

## 3 RESULTS

In this section, we will engage in a comprehensive discussion of filament length, delving into its cosmological implications and its

**Table 1.** This is an example table. Captions appear above each table. Remember to define the quantities, symbols and units used.

|                             | <i>ACDM</i> | P1      | P2      | C1        | I1        | SC1       | SI1       |
|-----------------------------|-------------|---------|---------|-----------|-----------|-----------|-----------|
| Box size [ $h^{-3} Mpc^3$ ] | 512         | 512     | 512     | 512       | 512       | 300       | 300       |
| Particle number             | $256^3$     | $128^3$ | $512^3$ | $256^3$   | $256^3$   | $512^3$   | $512^3$   |
| Cosmological parameters     | Same        | Same    | Same    | Different | Same      | Different | Same      |
| Initial condition           | Same        | Same    | Same    | Same      | Different | Same      | Different |
| Random seeds                | 50          | 5       | 5       | 5         | 5         | 5         | 5         |
| Total                       | 50          | 5       | 5       | 150       | 400       | 150       | 400       |

**Figure 1.** The critical points (bifurcation, node, saddle, and void) and filament segments are identified using DisPerSE. Saddle points serve to connect segments, forming complete filaments. Each complete filament connects two nodes or bifurcations, or links a cluster and bifurcation according to the cluster-filament-cluster configuration. Colors are utilized for distinguishing individual filaments.**Figure 2.** The filament length distributions derived from five numerical simulations in Planck15 cosmology with distinct initial distributions of matter evolving to  $z=0$ . Every filament length distribution statistic here is obtained using the filament pipeline mentioned in Sec.2 in a box of  $512(Mpc/h)^3$ . As can be seen, the cosmological fluctuation of the filament length distribution is very small, with only a small scatter in filaments longer than  $85Mpc/h$ .

relevance to cosmology. While filaments possess a multitude of properties such as width, shape, and more, we believe that length and mass contain a greater amount of information at larger scales, rendering them highly sensitive to the effects of cosmology and initial conditions. Previous studies have demonstrated a correlation between mass and length, allowing us to focus on the latter for this study [Cautun et al. \(2014\)](#). To begin, we analyze the variable parameters in the filament pipeline to investigate both cosmological fluctuations and filament length statistics. Following this, we examine the dependence of filament length and its evolution on cosmology and initial condition. Lastly, we elucidate the cosmological dependence of filament lengths through the use of a toy model.

### 3.1 Cosmic variance

The early universe displays uniform isotropy on a large scale, with tiny fluctuations on a smaller scale that give rise to filament and other large scale structures in later stages through gravitational interactions, as evident from the microwave background radiation. Furthermore, solving the Einstein-Boltzmann equation through numerical simulation enables us to determine the initial conditions of the universe, including the initial distribution of matter obtained through Gaussian sampling of the initial power spectrum. It should be noted that different random seeds of sampling produce different initial matter distributions can correspond to the same cosmological parameters, and if the filament length distributions exhibit less sensitivity to different cosmological parameters than to different initial matter distributions with the same cosmological parameters, it would pose a significant challenge to utilize filament length distributions for extracting cosmological information. In Fig. 2, we have analyzed the filament length distributions of 5 different initial distributions of matter at the  $z=0$  under the Planck15 cosmology with  $\Omega_m = 0.3075, \sigma_8 = 0.8158, n_s = 0.97, h = 0.667$ . Here the label of y axis on the upper panel  $\Phi_L$  is the number density of filament in each length bin.

$$\Phi_L = \frac{N}{V_{boxsize}} \quad (1)$$

where  $N$  is the number of filament in each length bin and  $V_{boxsize}$  is the box volume of the simulation. It is important to emphasize that all quantitative relationships in this article are derived using the number density  $\Phi_L$ . This choice aims to establish universal relationships independent of the box size. However, for the purpose of illustrating certain qualitative relationships, we occasionally use the exact number  $N$ . This decision is made under the consideration that, when the number  $N$  is less than 50, the impact of cosmological fluctuations becomes significant, and certain signals may be attributed to noise. We also define a transfer function  $T$  to describe the relative deviation for the statistic of physical quantity.

$$T = \frac{Q}{Q'} - 1 \quad (2)$$

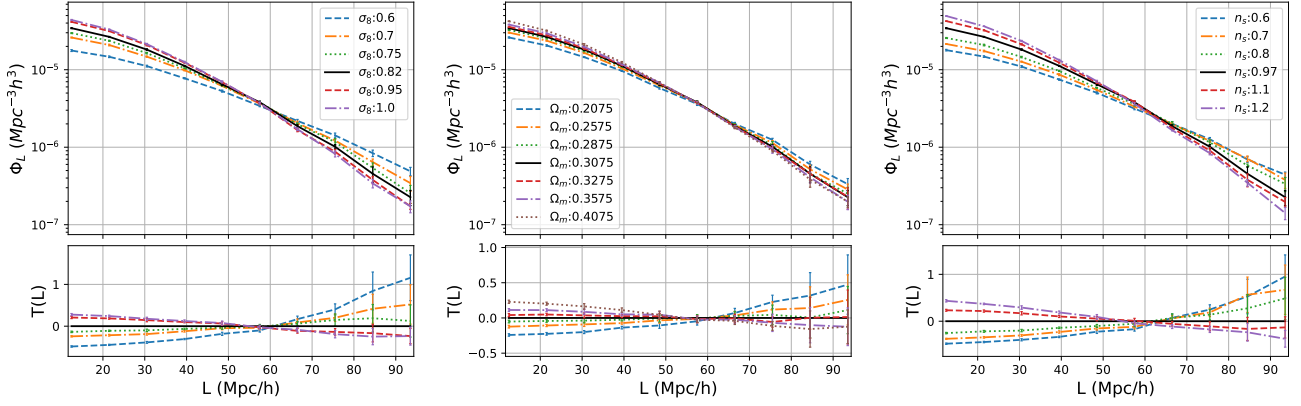


**Figure 3.** Filament length functions for different cosmologies computed from the filament pipeline with  $\Omega_m = 0.3075$ ,  $\sigma_8 = 0.82$ ,  $\omega = -1.0$ ,  $n_s = 0.97$  as standard cosmological parameters. The left, middle, and right panels present the differences of filament evolution functions for varying  $\sigma_8$ ,  $\Omega_m$ , and  $n_s$ , respectively. For each cosmology, we have calculated the filament length distribution from five different initial matter distributions. Our findings reveal that the filament length function varies with changing cosmological parameters, validating filament length function as a valuable cosmological probe.

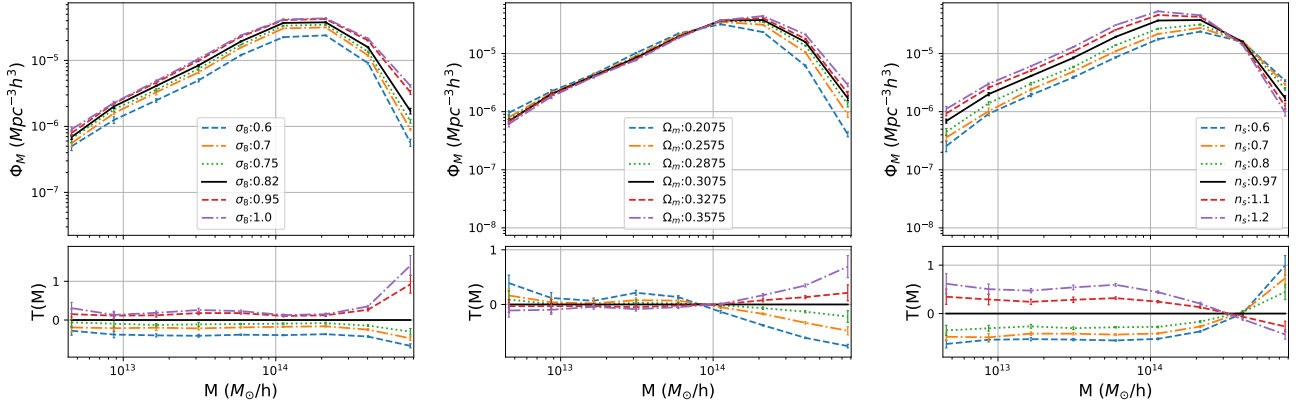


**Figure 4.** Filament mass functions for different cosmologies were computed using the filament pipeline with standard cosmological parameters set to  $\Omega_m = 0.3075$ ,  $\sigma_8 = 0.82$ ,  $\omega = -1.0$ , and  $n_s = 0.97$ . The left, middle, and right panels illustrate the variations in filament mass function due to changes in  $\sigma_8$ ,  $\Omega_m$ , and  $n_s$ , respectively. For each cosmology, the filament central mass distribution was calculated from five different initial matter distributions.

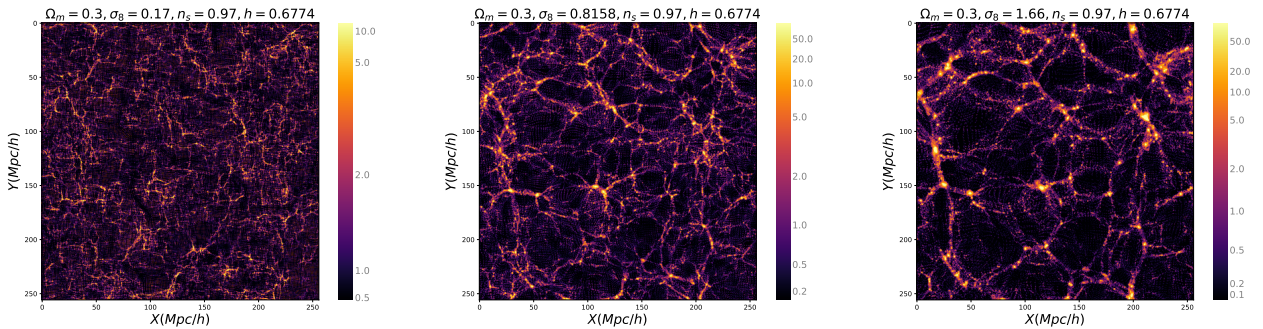


**Figure 5.** A slice of a particle mesh simulation obtained using pmwd in a  $256^3 (Mpc/h)^3$  box with  $256^3$  particles. The selected slice occupies a volume of  $16 * 256 * 256 (Mpc/h)^3$  and highlights the impact of varying  $\sigma_8$  on the large-scale structure of the Universe. As we progress from left to right in the figure,  $\sigma_8$  increases from 0.17 to 0.82 to 1.66, which leads to the development of more and more structures, such as clusters, as well as an increase in filament density. As the clustering grows more intense, filaments fragment into shorter ones, as observed in the figure.

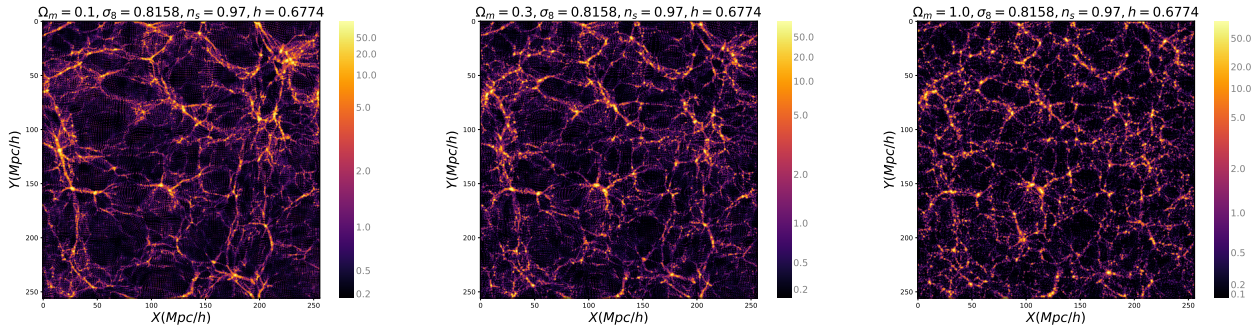


**Figure 6.** A slice of a particle mesh simulation obtained using pmwd in a  $256^3 (Mpc/h)^3$  box with  $256^3$  particles. The selected slice occupies a volume of  $16 * 256 * 256 (Mpc/h)^3$  and is displayed to showcase the impact of increasing  $\Omega_m$  on the large-scale structure of the Universe. As we move from left to right in the figure,  $\Omega_m$  increases from 0.1 to 0.3 to 1, and we observe the formation of more and more clusters. Additionally, an increasing number of longer filaments fragment into shorter ones due to the enhanced gravitational interactions.

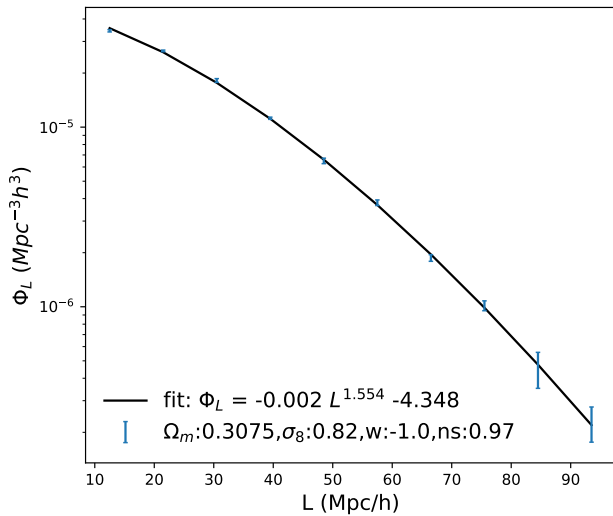


**Figure 7.** The filament length distribution for the Planck 15 cosmology at  $z = 0$  generated from five random seed values, represented by the blue dot with an error bar. The black line depicts the power law fitting, which exhibits very good fitting results. This fitting model efficiently captures the intrinsic relationship between filament mass and length, and serves as a valuable cosmological probe.

where  $Q$  is an arbitrary physical quantity and  $Q'$  is reference value of the physical quantity. The function  $T(L)$  represents the relative deviation for filament length distribution. The results show that the filament length distribution is not significantly influenced by the initial distribution of matter. This result supports the use of filament length distribution as a method to study cosmology.

### 3.2 Cosmological parameters

The large-scale structure distribution of the universe, including filaments, is influenced by various cosmological parameters, thereby affecting filament properties such as length and mass, which is the most straightforward and effective statistic for describing cosmological dependence of filament. Using the filament pipeline discussed in Sec. 2.1, we have investigated the relationship between filament length distribution and three different cosmological parameters. We found that filament length distribution exhibits varying degrees of

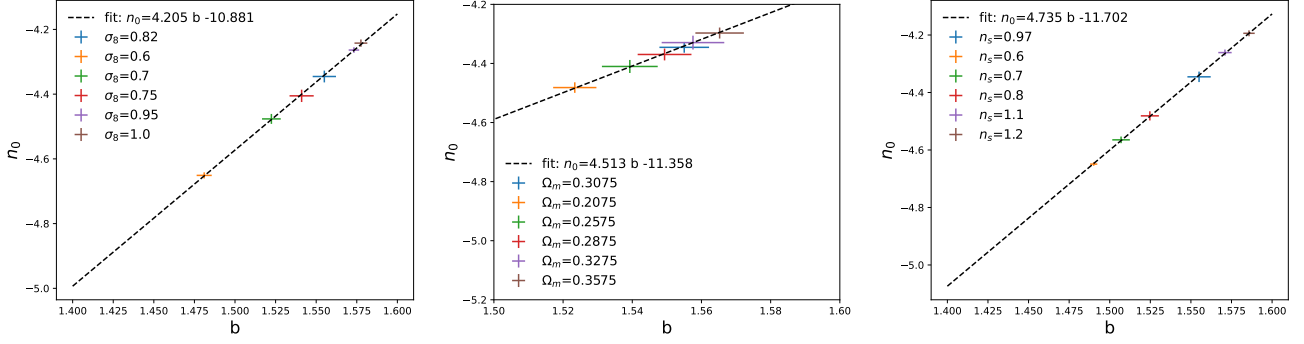
sensitivity to these three cosmological parameters, and the strength of this signal is significantly beyond the cosmological fluctuations.

Fig. 3 shows that as  $\sigma_8$  increases, the number of filaments, especially short ones, increases while the number of long filaments decreases on the left panel. The decrease of  $\sigma_8$  causes the universe to become more homogeneous, while an extremely low value of  $\sigma_8$  would leave the filament structure nearly empty. As  $\sigma_8$  increases and the clustering of each scale strengthens, more voids and peaks emerge, leading to an increase in the number of short filaments. However, as  $\sigma_8$  reaches higher values, additional peaks form within long filaments, potentially causing the fragmentation of longer filaments into smaller ones and consequently contributing to an elevated number of short filaments. To demonstrate this, we utilize the particle mesh algorithm to swiftly generate the cosmic structure of  $\sigma_8 = 0.16$ ,  $\sigma_8 = 0.82$ , and  $\sigma_8 = 1.6$  at  $z = 0$  in a  $256^3 (Mpc/h)^3$  box. This is illustrated in Fig. 5, where the absence of filamentary structure at low  $\sigma_8$  is notable, and an increase in the number of peaks with increasing  $\sigma_8$  indicates a greater presence of filamentary structure. When on the right panel of Fig. 3, increasing  $n_s$  has similar behavior as  $\sigma_8$ . For larger  $k$ , increasing  $n_s$  will increase the power on small scales, thus increasing the formation of peaks, so increasing the number of short filaments. But increasing of peaks also break long filament apart.

While an increase in  $\Omega_m$  weakens the clustering of large scale, the enhancement is not as obvious as  $n_s$ , resulting in a weaker change in filament length distribution shown on the middle panel of Fig. 3. This is understandable, that is the proportion of matter increases, leading to an increase of merging and therefore making it harder for extended structures to form, when  $\Omega_m = 1.0$ , in the extreme case, is the ED universe. We also demonstrate this with the particle mesh algorithm similar to Fig. 5 to generate the cosmic structure of  $\Omega_m = 0.1, \Omega_m = 0.3$  and  $\Omega_m = 1.0$ , as shown in Fig. 6, where many peaks shows and the extended structure is significantly reduced when the proportion of matter is large. The cosmological sensitivity of filament length distribution implies that it can serve as a useful cosmological probe.

Meanwhile, the abundance of filaments, measured in terms of length, exhibits a crossover at approximately  $60 Mpc/h$ . This specific value is subject to variation based on different parameter selections within the filament pipeline, such as  $N_{grid}$  and  $N_{smooth}$ . Nevertheless, this crossover point signifies a characteristic scale for filaments that warrants further exploration.

Furthermore, we calculate the filament central mass distribution, providing additional insights associated with the previously analyzed filament length distribution. The mass  $M$  here is determined through



**Figure 8.** In the phase space of power law fitting parameters  $n_0$  and  $b$  for the filament length distribution ( $\log_{10}\Phi_L = -0.002L^b + n_0$ ), we observe a linear relationship among different cosmological parameters, as demonstrated in the figure. For each cosmology, five simulations with distinct initial matter distributions were used, and the cosmic variance for  $n_0$  and  $b$  values has been illustrated. As evident from the left and right panels, the relation is tighter for  $\sigma_8$  and  $n_s$ , while the relation for  $\Omega_m$  on the middle panel exhibits lower precision.

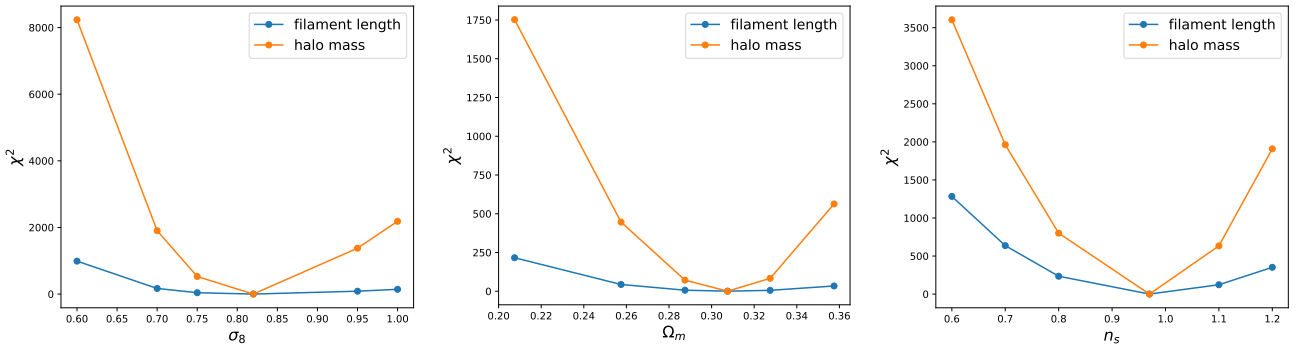


**Figure 9.** Conditional constraints on  $\sigma_8$ ,  $\Omega_m$  and  $n_s$ , derived using halo mass function and filament length function. Estimation is based on the simulation of 118 COLA simulation with a boxsize of  $512 (Mpc/h)^3$ . The result indicates that the filament length function is slightly less stringent in terms of cosmological constraints compared to the halo mass function.

linear interpolation along the filament stem in the density field. In Fig. 4, the filament mass distribution with varying cosmological parameters ( $\sigma_8$ ,  $\Omega_m$ ,  $n_s$ ) is presented from left to right. In the left panel, we observe that a larger  $\sigma_8$  leads to an increase in filament mass across all mass ranges. Comparing this with the filament length distribution, we note that shorter filaments in a larger  $\sigma_8$  scenario may exhibit a higher central density, compensating for the deficiency in long filaments.

Moving to the middle panel, an increase in  $\Omega_m$  results in a completely inverse relationship between filament mass distribution and filament length distribution. Specifically, the number of short filaments tends to increase, while low-mass filaments decrease. Simultaneously, the number of long filaments tends to decrease, but high-mass filaments increase. This implies that, with an increase in  $\Omega_m$ , long filaments tend to have lower central density, while short filaments tend to have higher density. This aligns perfectly with our earlier conjecture: the increase in  $\Omega_m$  leads to the emergence of peaks, strengthening short filaments, while extended filaments need to maintain low density to avoid generating new peaks. Regarding  $n_s$ , the variations in filament mass distribution originate from changes in filament length distribution, as they exhibit the same tendency.

Here we use Eq. 3 to fit the filament length distribution and get a nice fitting as shown in Fig. 7.

$$\log_{10}\Phi_L = -0.002L^b + n_0 \quad (3)$$

We have applied a fitting model to the distribution of filament

lengths for varying cosmological parameters such as  $\sigma_8$ ,  $\Omega_m$ , and  $n_s$ . Through this fitting process, we have observed a linear relationship in the parameter space of  $b$  and  $n_0$  as shown in Fig. 8.

We also compare the sensitivities of the filament length function and the halo mass function to different cosmological parameters. To determine the halo mass function, we use the Friends-of-Friends (FOF) method to identify halos in our simulations and then take statistics of their masses. We take two bins of halo mass between  $M \in [13, 15]M_\odot$  as the statistics for this analysis. Similarly, we use the fitting parameters of filament length  $b$  and  $n_0$  as the statistics for the filament length function. We defined a statistical function:

$$\chi^2 = (\mathbf{p}_{\text{fiducial}} - \mathbf{p}_{\text{target}}) \cdot \mathbf{Cov}^{-1} \cdot (\mathbf{p}_{\text{fiducial}} - \mathbf{p}_{\text{target}}) \quad (4)$$

For our analysis, we adopt the Planck 15 cosmology with parameters  $\Omega_m = 0.3075$ ,  $\sigma_8 = 0.82$ , and  $n_s = 0.97$  as the fiducial geometric background. We use 40 simulations from the COmoving Lagrangian Acceleration (COLA) framework to calculate the covariance matrix, and denote the fitting parameters for the halo mass function and filament length as  $\mathbf{p}$ .

Our results in Fig. 9 show that the halo mass function is more sensitive to cosmological variations than the filament length function. However, due to the strong measurement uncertainty associated with the halo mass function, the filament length function still holds great potential as a cosmological probe.

To examine the robustness of the filament length distribution as

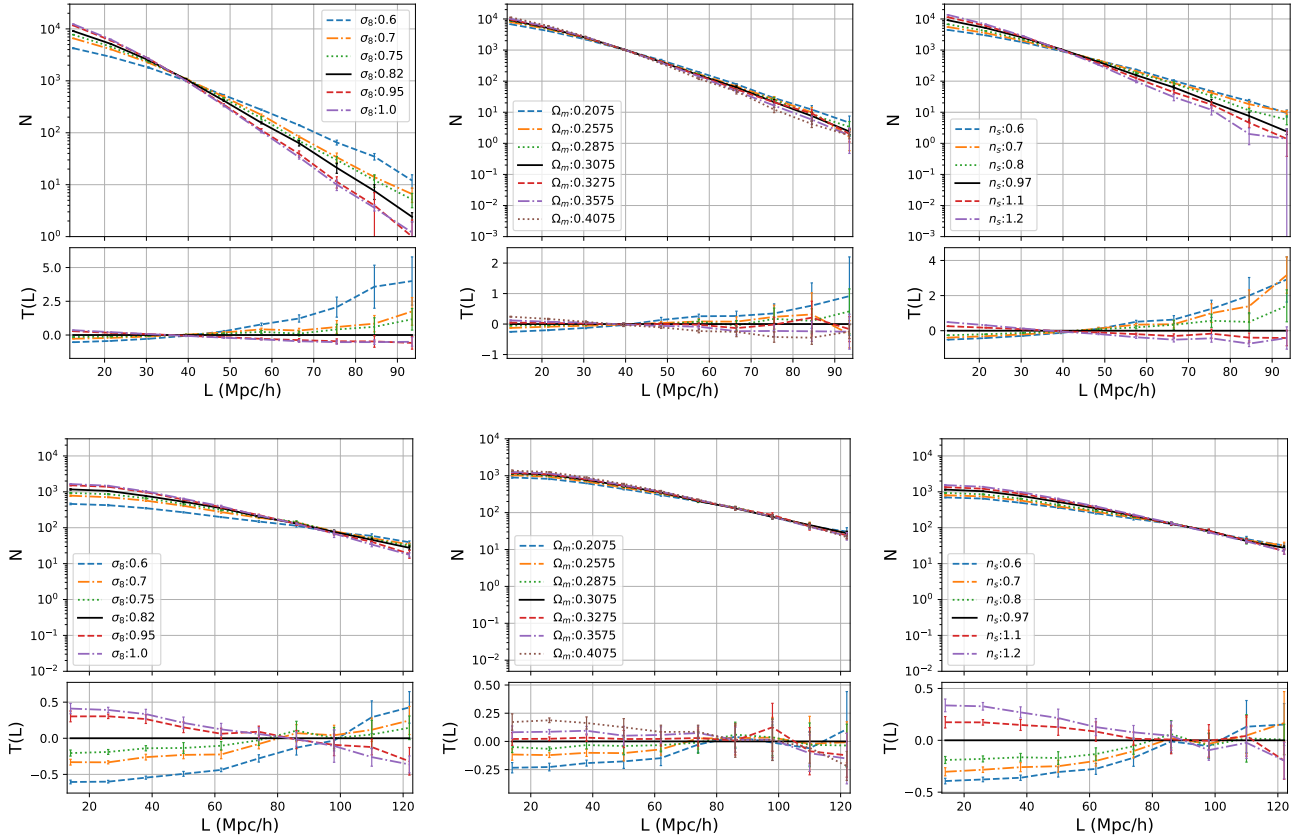


**Figure 10.** Filament length distribution computed from the filament pipeline for different cosmologies, using either a small lattice number  $N_{grid}$  or a large smooth scale  $N_{smooth}$ . The left, middle, and right panels display the filament evolution functions for varying  $\sigma_8$ ,  $\Omega_m$ , and  $n_s$ , respectively. The top panel shows the length distributions based on the coarse density field with  $N_{grid} = 128$ , while the bottom panel presents the length distributions based on the density field with  $N_{smooth} = 3(Mpc/h)$ . For each cosmology, we have calculated the filament length distribution using five different initial matter distributions. Our findings illustrate that neither a small  $N_{grid}$  nor a large  $N_{smooth}$  will erase the cosmological signal in the filament length function, demonstrating its robustness as a valuable cosmological probe. Furthermore, a small  $N_{grid}$  implies that even with imprecise galaxy positions, we can still obtain useful constraints on cosmological parameters through the filament length function.

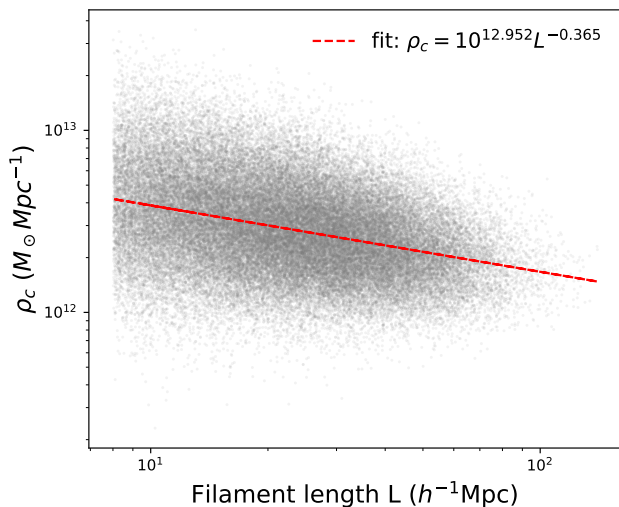


**Figure 11.** Filament mass and length relation in Planck 15 cosmology at  $z = 0$ . The red line is the power law fitting which shows a power law relation between filament mass and length.

a cosmological probe, we have applied the same research methods to a coarse field generated by the same simulation used in our previous analysis. We have tested two different settings, one with  $N_{grid} = 128$  and no smoothing, and the other with  $N_{grid} = 512$  and  $N_{smooth} = 3Mpc/h$ . To facilitate the observation of the actual filament numbers, we have refrained from dividing the box size, given that both measurements are based on a common volume of  $512(Mpc/h)^3$ . The former setting helps us assess whether the observation precision limits may obscure the cosmological signal, while the latter setting helps us investigate the robustness of the signal. As depicted in Fig. 10, our findings suggest that neither the lattice number nor the smoothing scale can erase the cosmological signal under reasonable conditions, indicating that the filament length function is a highly robust cosmological probe.

As filament mass and length exhibit a correlation, we have also explored the intrinsic relationship between mass and length, and its cosmological dependence. By employing the topological DisPerSe method for filament identification, we acquire the filament stems. Subsequently, the central density  $\rho_c$  is determined by linear interpolation along the filament stem in the density field. It is calculated as the ratio of the previously mentioned filament mass  $M$  to the filament length  $L$ , offering a one-dimensional measure that excludes radius

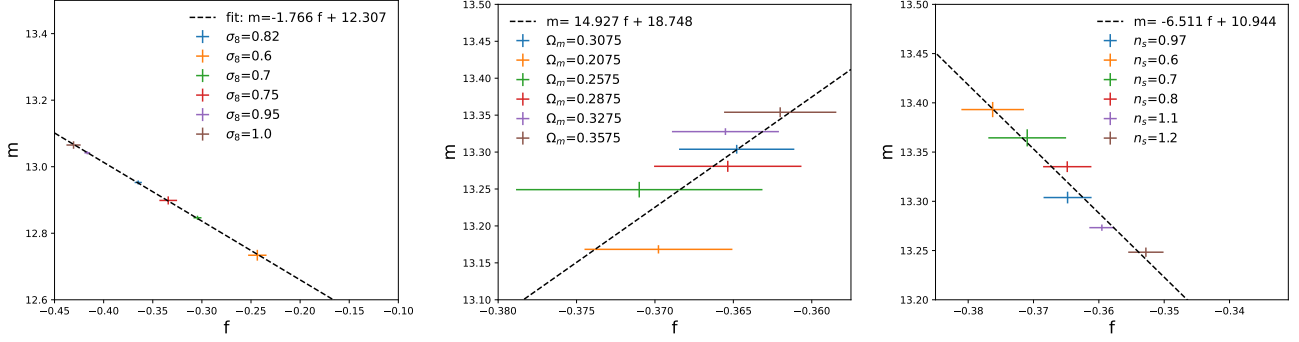


**Figure 12.** The relation of power law fitting parameters  $a$  and  $b$  in filament central density and length relation  $\rho_c = 10^m \times L^f$ . The figure shows that different cosmological parameters obey a linear relation in the power law fitting parameters phase space. 5 simulations with different initial matter distribution have been used for each cosmology and the cosmic variance for  $f$  and  $m$  has been shown. The relation is tighter for  $\sigma_8$  showing on the left panel and not very tight for  $om$  and  $ns$  on the middle and right panel respectively.

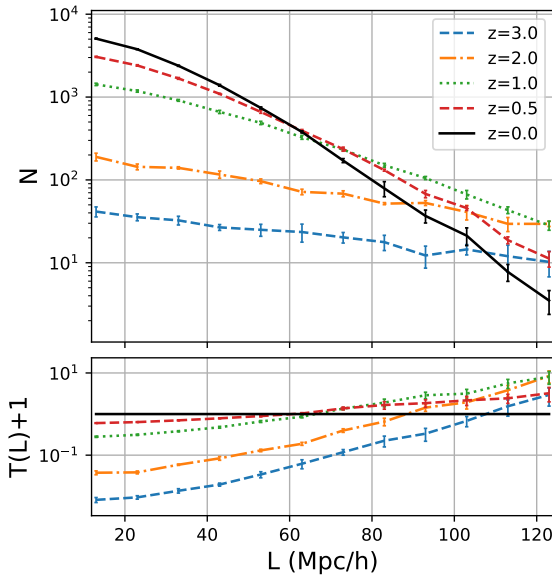


**Figure 13.** Filament length distributions for different redshift as well as their ratio to  $z = 0$  in Planck15 cosmology.

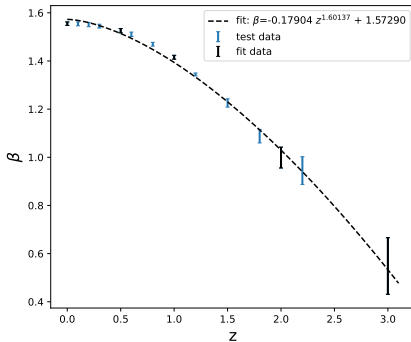


**Figure 14.** The relationship between the power law index  $\beta$  in the filament length function and redshift can be effectively described by the equation  $\beta = az^f + b$ . The black dots represent 5 redshift used for fitting this relationship, while the blue dots represent the redshift that can be accurately predicted by the fitting relation.

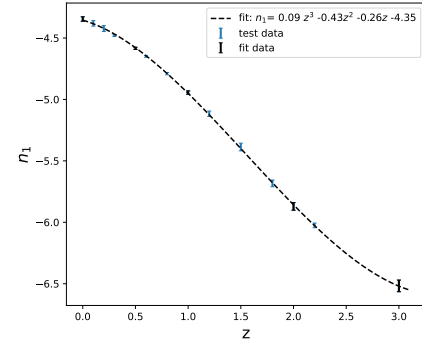


**Figure 15.** The relationship between the parameter  $n$  in the filament length function and redshift can be effectively described by a cubic function. The black dots represent 5 redshift used for fitting this relationship, while the blue dots represent the redshift that can be accurately predicted by the fitting relation.

information. In mathematical terms:

$$\rho_c = \frac{M}{L} \quad (5)$$

Our findings reveal a power-law relationship between filament central density  $\rho_c$  and length  $L$  in the context of Planck 15 cosmology, as depicted in Fig. 11. It indicates that longer filaments tend to display lower density. Furthermore, we have found that the power law relation between filament central density and length holds for varying cosmological parameters and that the fitting parameters  $f$  and  $m$  in the power law relation  $\rho_c = 10^m \times L^f$  exhibit a linear relationship for different cosmologies, as demonstrated in Fig. 12. Our findings suggest that the parameter  $f$  can be employed to distinguish between different  $\sigma_8$  values, whereas distinguishing between different  $\Omega_m$  and  $n_s$  values with high cosmic variance is more difficult, even though they exhibit a nearly linear relationship in the parameter space. Therefore, we can leverage the power law fitting phase space relation to constrain the cosmological parameters in question. And this implies that varying  $\sigma_8$  can exert a significant impact on the central density of filaments. A higher value of  $\sigma_8$  leads to increased clustering, resulting in shorter filaments having higher central density. Conversely, the parameters  $\Omega_m$  and  $n_s$  produce the opposite effect. Given the inherent challenges in accurately measuring mass through observations, additional research and analysis are needed to

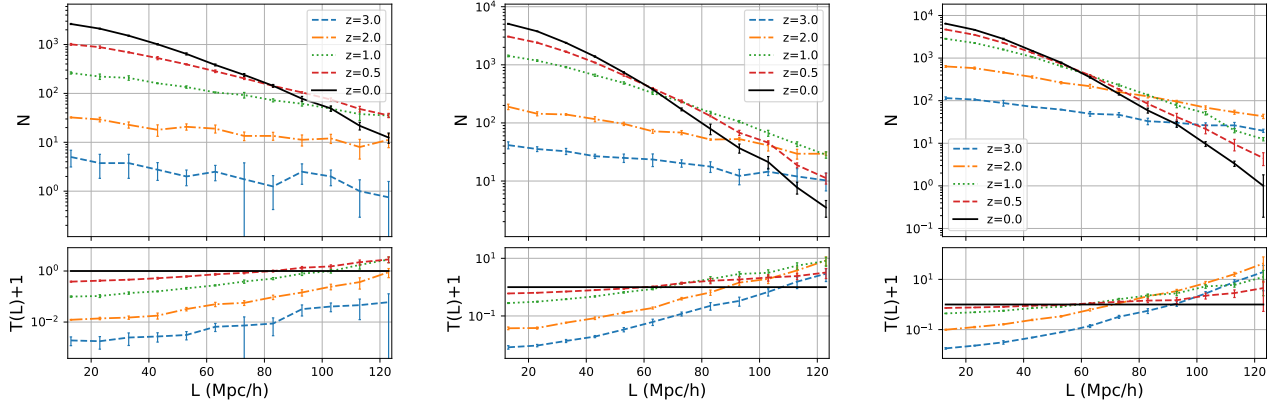


**Figure 16.** The effects of different  $\sigma_8$  cosmologies at  $\sigma_8 = 0.60, 0.82, 1.0$  from left to right on filament formation by comparing the filament length distributions and their ratios relative to  $z = 0$  at different redshifts. Our results demonstrate that varying  $\sigma_8$  leads to changes in the filament formation process.

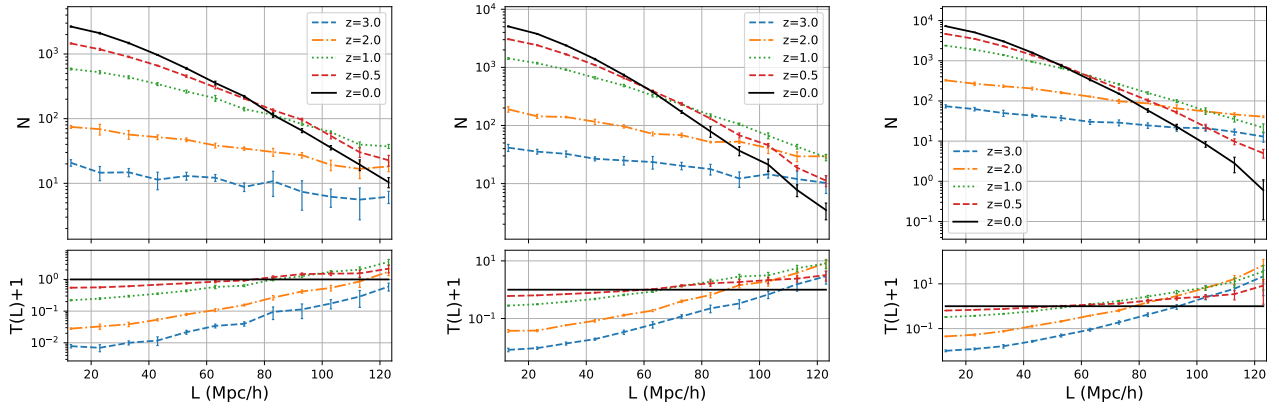


**Figure 17.** The effects of different  $n_s$  cosmologies at  $n_s = 0.60, 0.97, 1.20$  from left to right on filament formation by comparing the filament length distributions and their ratios relative to  $z = 0$  at different redshifts. Our results demonstrate that varying  $n_s$  leads to changes in the filament formation process.

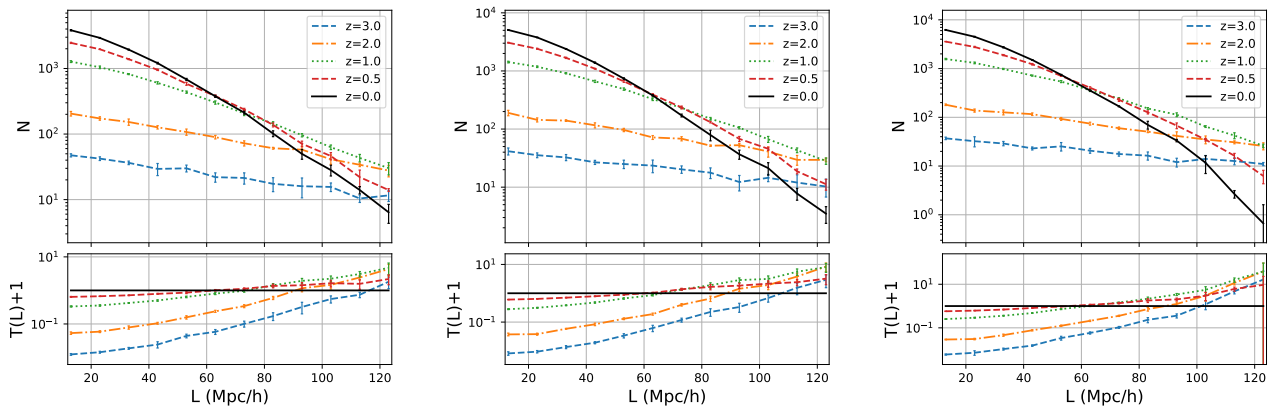


**Figure 18.** The effects of different  $n_s$  cosmologies at  $\Omega_m = 0.2075, 0.3075, 0.4075$  from left to right on filament formation by comparing the filament length distributions and their ratios relative to  $z = 0$  at different redshifts. Our results demonstrate that varying  $\Omega_m$  leads to little changes in the filament formation process.

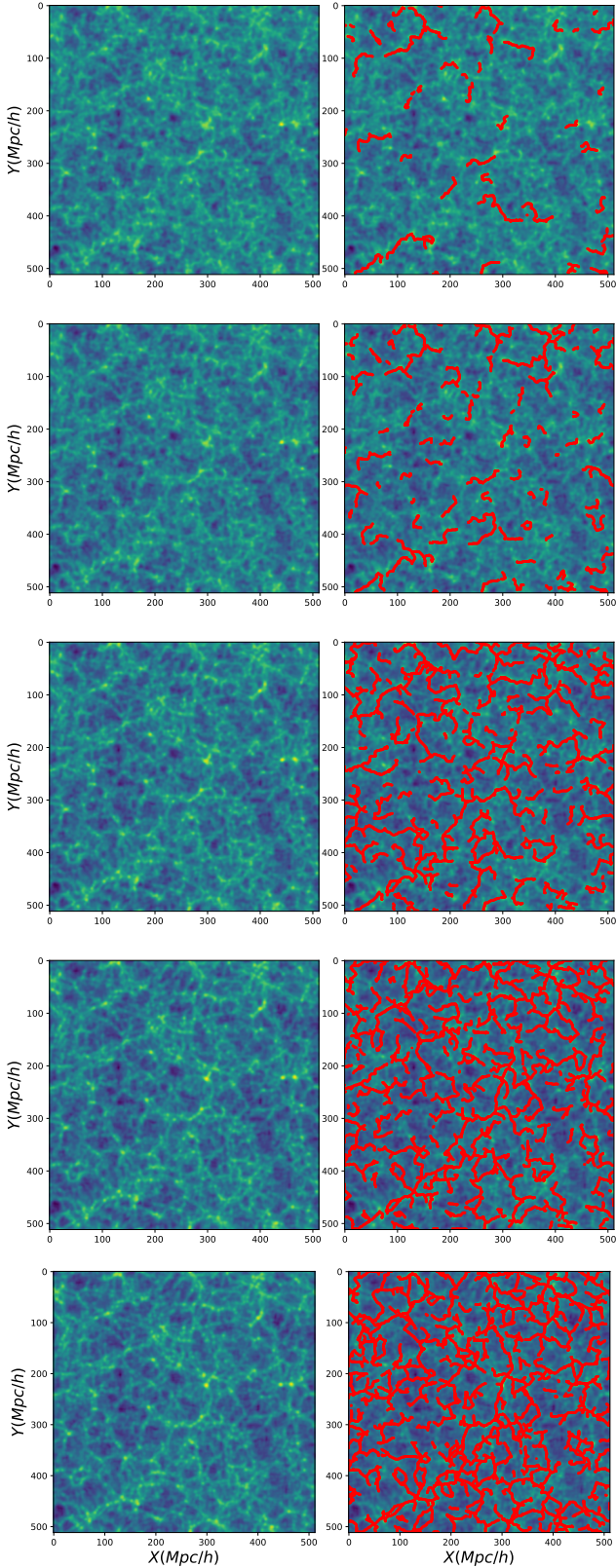


**Figure 19.** Visual comparison for different redshift in Planck15 cosmology. A slice of the density field with size of  $20 * 512 * 512 (Mpc/h)^3$  with  $z = 3, 2, 1, 0.5, 0$ . from top to bottom on the left panel and the filament found by DisPerSe with the corresponding redshift on the right panel.

further explore the application of this probe in constraining cosmological parameters.

### 3.3 Reshift evolution

We have also investigated whether the evolution of filaments is sensitive to cosmology, specifically whether the distribution of filament lengths changes with redshift in a cosmologically meaningful way. To perform this analysis, we preserved 5 redshift snapshots in our numerical simulation:  $z = 3, 2, 1, 0.5, 0$ . We obtained the filament length distributions for each snapshot using our filament pipeline and present the results in Figure 13, using the Planck15 cosmology as a reference. Our analysis reveals that as redshift increases, the number of filaments with different lengths grows until  $z \sim 1$ , after which the number of long filaments decrease while the number of short filaments increases. These findings diverge from those presented in a prior study by Cautun et al. (2014), which yielded nearly the opposite outcome, indicating more long filaments and fewer short filaments at low redshifts. This disparity is reasonable, considering that their filament definition relied solely on the bifurcation and curvature of the filament, leading to ignoring the process when peaks show up and break down the filament into two parts in contrast to our definition. Visual comparison is utilized to compare the filamentary structure detected in different redshift in Fig. 19. Our findings suggest that filament formation have 3 steps: 1) as redshift decreases, an increasing number of filaments form, some of which connect to form more extensive structures. 2) After  $z \sim 2$ , the longest filaments have already formed and remain unchanged until  $z \sim 1$ . 3) After this point, matter becomes more clustered, causing some long filaments to break apart and shorter filaments to become more prevalent.

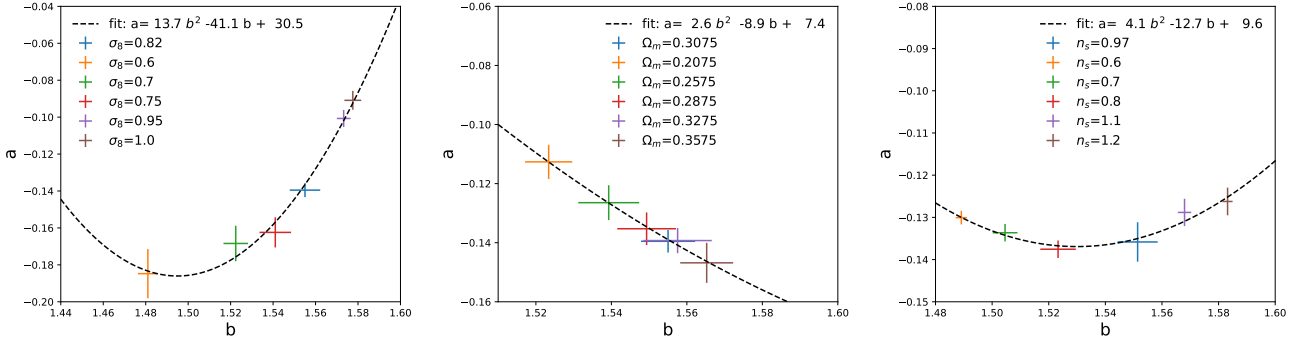
Furthermore, we have discovered that Eq. 6 can be employed to accurately fit the redshift dependency of the filament length function.

$$\log_{10}\Phi_L = -0.002L^\beta + n_1, \quad \beta = a * t^z + b \quad (6)$$

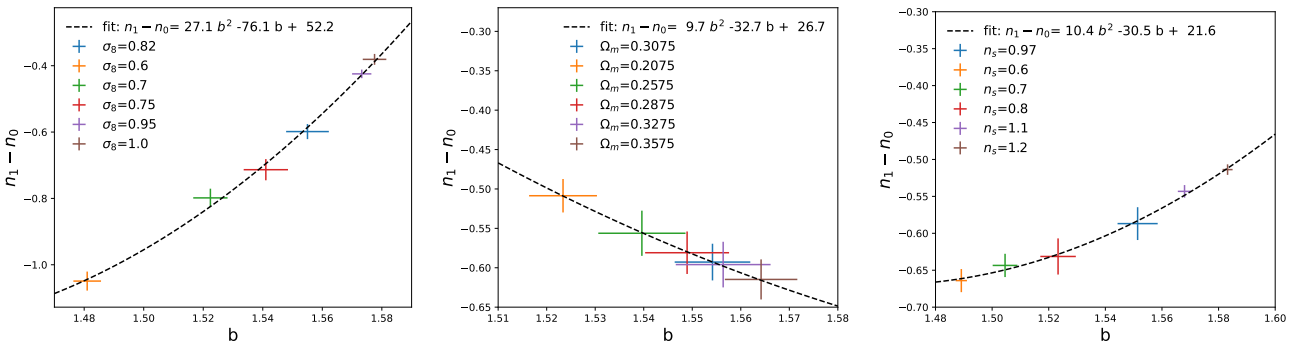
where  $\beta$  will be shown in Fig. 14. Specifically, the power law index in the filament length function exhibits a power law relationship with redshift. By utilizing five redshift values for fitting the power law index and redshift relationship, we successfully predict the behavior for another set of five redshift values. This indicates that the fitting function effectively describes the power law index and its relation to redshift. The corresponding results are presented in Fig. 14. Furthermore, we determine that the relationship between  $n_1$  and redshift can be suitably approximated by a cubic function, as depicted in Fig. 15. Combining these two relations, we gain an approximate understanding of filament evolution. We propose a straightforward model by dividing the filament into two distinct components: long filaments and short filaments. Under the assumption that long filaments are formed through the merging of shorter ones, we can observe a simplified evolution pattern for filaments. This model suggests that the formation of short filaments is driven by density growth. Simultaneously, short filaments contribute to the development of long filaments, while local density enhancements cause the fragmentation of long filaments into shorter segments. In essence, this model can be represented by Fig. 31.

Fig. 31 depicts the formation and transformation of short and long filaments. The (F) process corresponds to the filament forming process resulting from density perturbations, while (B) signifies the breaking down process from long filaments to shorter ones. Additionally, (G) represents the growth process from short filaments to long filaments.

Prior to a redshift of 2, the  $\beta$  value remains below 1, indicating



**Figure 20.** In the phase space of power law fitting parameters  $a$  and  $b$  for the filament length distribution ( $\log_{10}\Phi_L = -0.002L^{a \cdot z + b} + n_1$ ), we observe a linear relationship among different cosmological parameters, as demonstrated in the figure. For each cosmology, five simulations with distinct initial matter distributions were used, and the cosmic variance for  $a$  and  $b$  values has been illustrated, indicating the process filament change from short to extensive at low redshift.



**Figure 21.** In the phase space of power law fitting parameters  $n_1 - n_0$  and  $b$  for the filament length distribution ( $\log_{10}\Phi_L = -0.002L^{a \cdot z + b} + n_1$  and  $\log_{10}\Phi_L = -0.002L^b + n_0$ ), we observe a linear relationship among different cosmological parameters, as demonstrated in the figure. For each cosmology, five simulations with distinct initial matter distributions were used, and the cosmic variance for  $n_1 - n_0$  and  $b$  values has been illustrated, indicating the amount of filament form at low redshift.

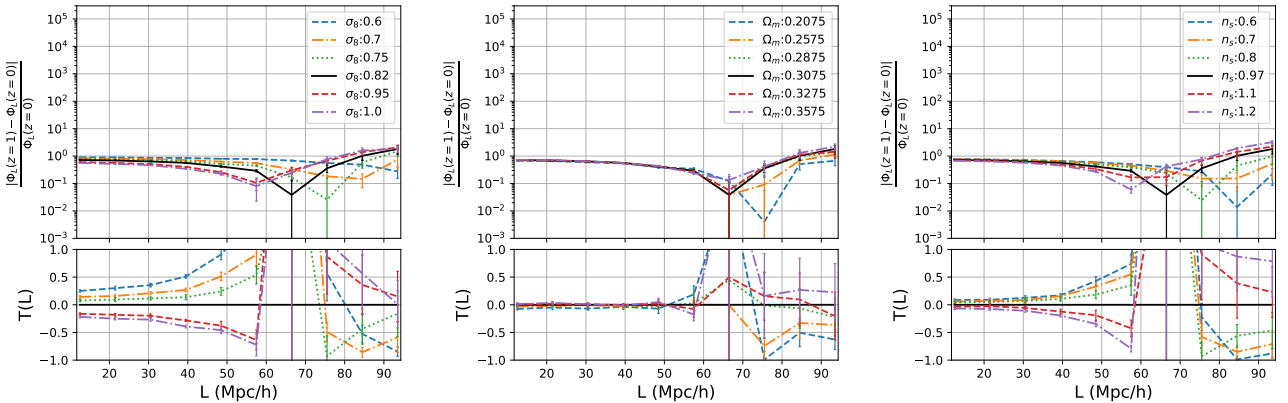


**Figure 22.** Filament evolution function for different cosmology. The difference of filament length distribution between  $z = 0$  and  $z = 1$  has shown in this figure. From the left panel to the right panel, the difference of filament evolution function for different  $\sigma_8$ ,  $\Omega_m$  and  $n_s$  have shown respectively.

a relatively small difference between the numbers of long and short filaments. During this period, the dominant processes are forming (F) and growth (G), while breaking down (B) processes are minimal. However, as the redshift approaches  $z = 2$ , the  $\beta$  value converges towards 1. The increasing slope of  $n_1$  suggests a significant augmentation in the forming process (F), accompanied by a reduction in the

growth process (G). At around  $z = 1.5$ , the slope of  $n_1$  reaches its maximum, indicating the peak of the forming process (F). Subsequently, the growth process (G) decreases, while the breaking down process (B) intensifies. The analysis provides a physical explanation of the three stages of the filament forming process. Worth noting is that the formation of filaments is a consistently dynamical process.

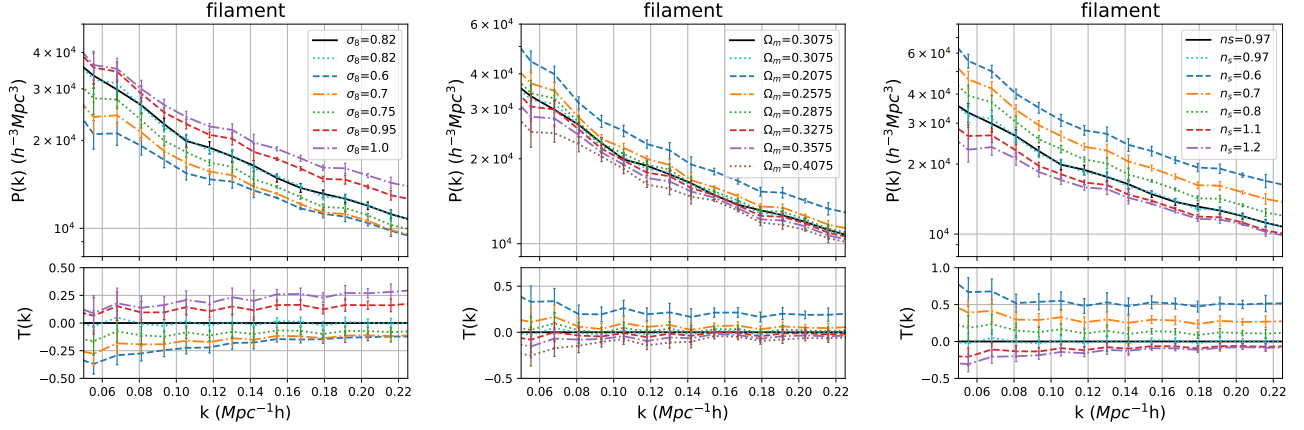


**Figure 23.** The power spectrum of dark matter particles for different  $\sigma_8$ ,  $\Omega_m$ , and  $n_s$  respectively. The black lines shows the Planck15 cosmology using 40 initial random seed and the other use 5 initial random seed. Our estimation is based on simulations of 118 COLA runs using a box size of  $512 (Mpc/h)^3$ .

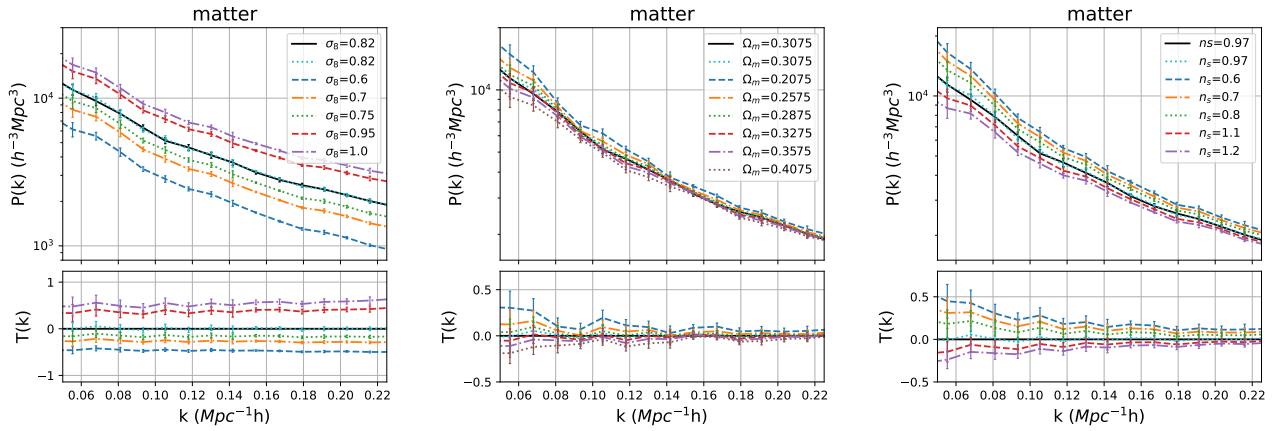


**Figure 24.** The power spectrum of dark matter particles inside filaments for different  $\sigma_8$ ,  $\Omega_m$ , and  $n_s$  respectively. The black lines shows the Planck15 cosmology using 40 initial random seed and the other use 5 initial random seed. Our estimation is based on simulations of 118 COLA runs using a box size of  $512 (Mpc/h)^3$ .

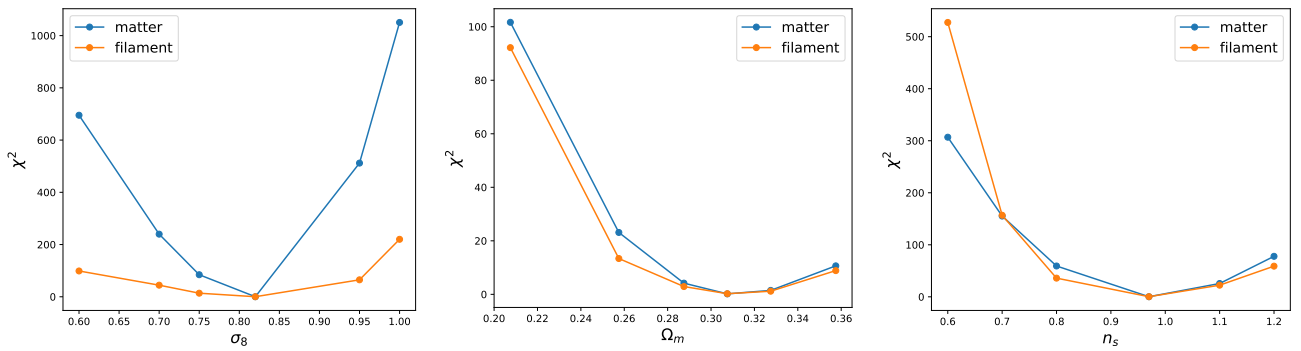


**Figure 25.** Conditional constraints on  $\sigma_8$ ,  $\Omega_m$ , and  $n_s$  by analyzing the power spectrum of dark matter particles and those inside filaments. Our estimation is derived from simulations comprising 118 COLA runs, utilizing a box size of  $512 (Mpc/h)^3$  (with 40 runs dedicated to covariance matrix calculations). The statistical function  $\chi^2$  is computed to assess the sensitivity to various cosmological parameters, comparing results obtained from all particles with those from particles located within filaments. Our findings suggest that utilizing the particles inside filaments can yield stronger constraints on cosmology for some cosmological parameters like  $n_s$ .

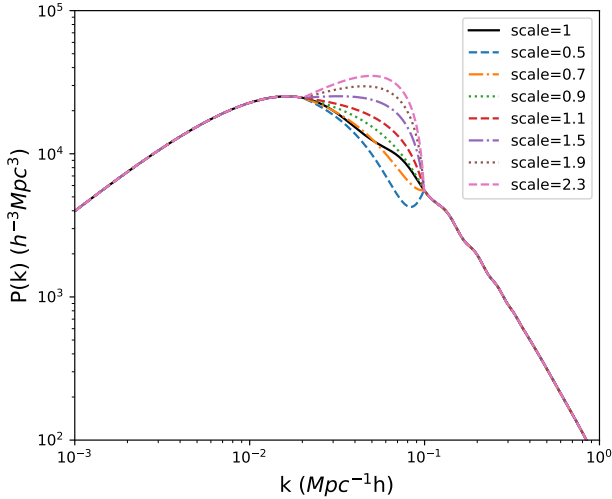


**Figure 26.** The initial power spectrum we generate in one of the intervals  $k \in [0.02, 0.1]$  with different amplitudes.

This is in sharp contrast with the abundance of density peaks that ultimately form halos, which is little changed with dynamical evolution under self-gravity. In fact, the abundance of halos at any redshift can be well described by the so-called halo model, given the initial condition and cosmological growth factor are known. Moreover, the two-point correlation function of large halos or rare density peaks is a very weak function of redshift, and is largely pre-determined by the heights of density peaks in the gaussian density field. Thus, one may recap the following overall physical that is emerging from our analysis of filaments, in conjunction with our previously known knowledge about the formation and evolution of halos: the large nodes in the cosmic web that are destined to form massive halos such as groups or clusters of galaxies are imprinted in the initial density field and can be calculated without the need of simulations, whereas the evolution of filaments that connect the nodes is more complex, which does not have an equivalent tool, such as the halo model. The analysis presented here provides very useful insight for not only this dynamical process but also potential cosmological applications of filaments.

Moreover, the parameter  $b$  is derived from the fitting value at  $z = 0$ , and we establish the value of parameter  $n_1$  at  $z = 0$  as  $n_0$ . Therefore, we can observe that the parameters  $n_1 - n_0$  serve to define the length of intersection for the filament within a given redshift and  $z = 0$ . Meanwhile, the parameter  $a$  indicates the change in the normalized filament length distribution with respect to different redshift. An increase in the parameter  $a$  corresponds to filaments becoming more extensive and occupying a larger portion within the distribution. This suggests a transition from shorter filaments to more extensive ones. Furthermore, an increase in the parameter  $n_1 - n_0$  leads to the appearance of not only shorter filaments but also extensive ones, thereby increasing the overall presence of filaments.

Furthermore, we have used our filament pipeline to explore how the filament length distribution evolution varies with different cosmological parameters. We investigate the change in the filament length distribution as three cosmological parameters,  $\sigma_8$ ,  $\Omega_m$  and  $n_s$  respectively. As Figure 16 indicates, increasing  $\sigma_8$  leads to accelerated filament formation, with each step occurring at a higher redshift. Similar results were obtained for  $n_s$ , as demonstrated in Fig. 17.

However, we do not observe significant changes in filament formation for different  $\Omega_m$  cosmologies, as evidenced by our analysis shown in Fig. 18. Meanwhile, Our analysis also revealed that regardless of the cosmological parameters, the number of filaments of each length increases as redshift decreases from 3 to 2.

However, when we shift our focus to low redshifts, we observe a decrease in the number of extensive filaments, with shorter filaments becoming more predominant. To examine the filament's evolutionary behavior, depicted in Figure 22, we varied three cosmological parameters: specifically,  $\sigma_8$ ,  $\Omega_m$ , and  $n_s$ . Utilizing the formula 3, we fitted all the cosmological simulation data and plotted the results in Figure 20 and Figure 21. Remarkably, we discovered that a quadratic function could effectively fit both the parameter  $a$  and  $n_1 - n_0$ . Analyzing the influence of  $\sigma_8$ , we observed that as it increased, the parameter  $a$  also grew larger, suggesting an increased formation of extensive filaments at low redshifts. Turning our attention to  $n_1 - n_0$ , we noticed that its value increased with a higher  $\sigma_8$ , indicating a reduced occurrence of filaments. This correlation can be attributed to the fact that a larger  $\sigma_8$  corresponds to stronger clustering properties, resulting in the formation of more filaments at higher redshifts and an increased presence of extensive filaments at lower redshifts. Conversely, increasing  $\Omega_m$  yielded the opposite effect. Both  $a$  and  $n_1 - n_0$  decreased, implying that a higher matter density may cause extensive filaments to break up at low redshifts, while filament formation remains active. Comparing different values of  $n_s$ , we observed similar trends to  $\sigma_8$ , except for a notable deviation near the standard cosmology value of 0.97 for the parameter  $a$ . This suggests a transition from short filaments to longer ones at low redshifts for different  $n_s$  values near the standard cosmology.

### 3.4 Correlation function

The two-point correlation function stands out as one of the most frequently employed statistics for characterizing a homogeneous density field,

$$\xi(\mathbf{r}) = \langle \delta(\mathbf{x}) \delta(\mathbf{x} + \mathbf{r}) \rangle, \quad (7)$$

where  $\delta(\mathbf{x})$  is the density contrast field,  $\mathbf{x}$  denote for any point,  $\mathbf{r}$  is a separation vector, and  $\langle \cdot \rangle$  stands for the ensemble mean, computed with a spatial mean over  $\mathbf{x}$  in practice.

While the anisotropic two-point correlation function (2PCF), denoted as  $\xi(\mathbf{r})$ , serves as a measure of galaxy clustering using the standard estimator proposed by Landy & Szalay (1993), it is expressed as:

$$\xi(r, \mu) = \frac{DD(r, \mu) - 2DR(r, \mu) + RR(r, \mu)}{RR(r, \mu)} \quad (8)$$

where  $DD$ ,  $DR$ , and  $RR$  are the normalized galaxy-galaxy, galaxy-random, and random-random number of pairs with separation  $(r, \mu)$ , respectively. The 3D separation vector between pairs of objects, denoted as  $\mathbf{r}$ , has been decomposed into coordinates  $(r, \mu)$ , where  $r$  is the norm of the separation vector, and  $\mu$  is the cosine of the angle between the line-of-sight and the separation vector directions.

The power spectrum of  $\delta(\mathbf{x})$  is just related to  $\xi(\mathbf{r})$  by the Fourier transform, i.e.,

$$P(\mathbf{k}) = \int \xi(\mathbf{r}) e^{i\mathbf{k} \cdot \mathbf{r}} d^3 \mathbf{r} \quad (9)$$

where  $\mathbf{k}$  is the 3D wavevector of the plane wave, with the magnitude  $k \equiv |\mathbf{k}|$  (the wavenumber) related to the wavelength  $\lambda$  by  $k = 2\pi/\lambda$ .

These two methods serve as valuable tools for conducting statistical analyses on the large scale of the universe, enabling the constraint

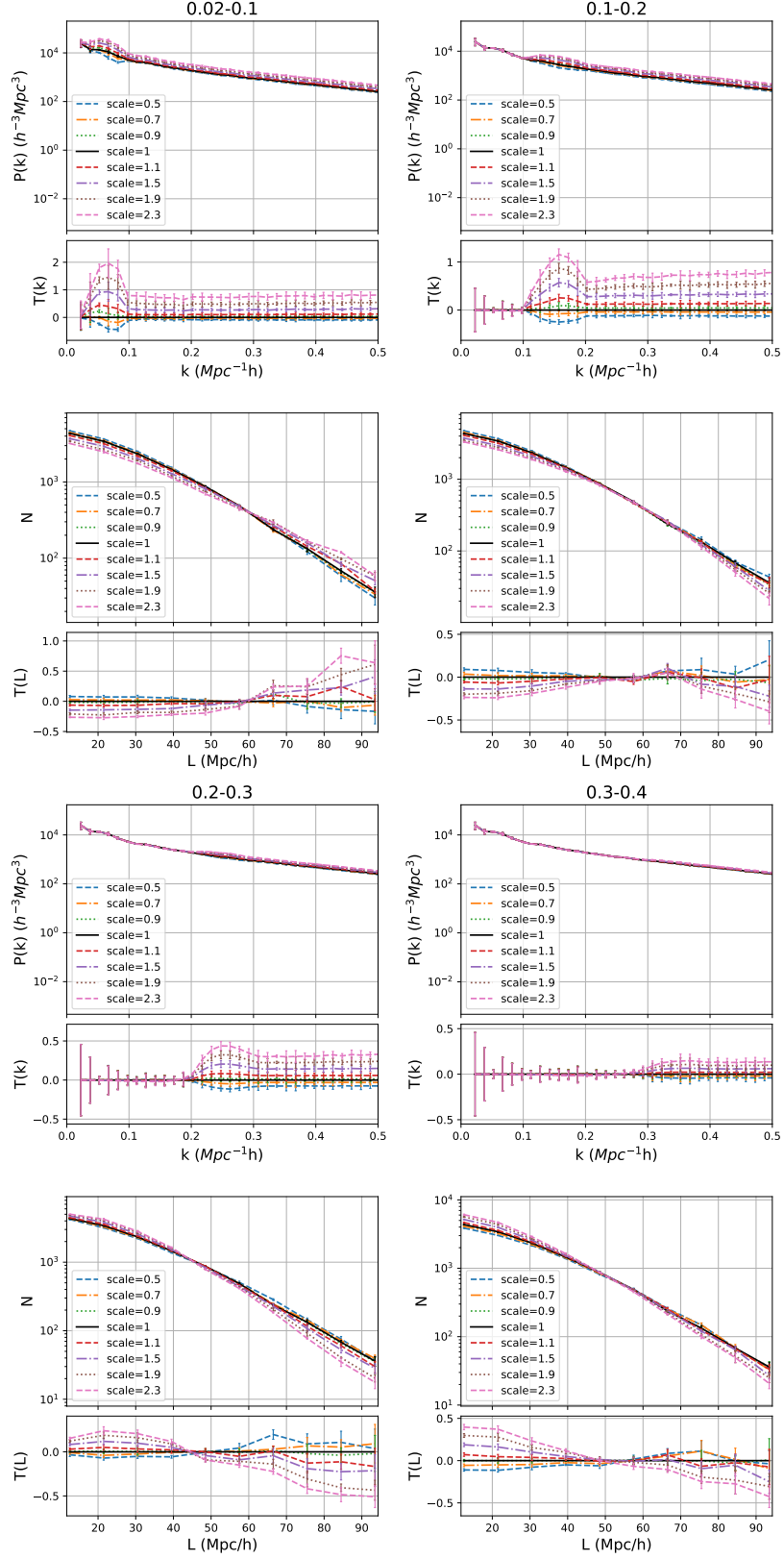


**Figure 27.** Comparison of the modified power spectra at  $z = 0$  and the filament length function. The fluctuations at different scales  $k \in [0.02, 0.1, 0.2, 0.3, 0.4]$  lead to changes in the formation of filaments and the large-scale structure. The first row displays the obtained power spectra, with each column corresponding to a different scale modification. The second row exhibits the corresponding filament length distribution, illustrating how modifications to the initial power spectrum affect the formation of filaments.

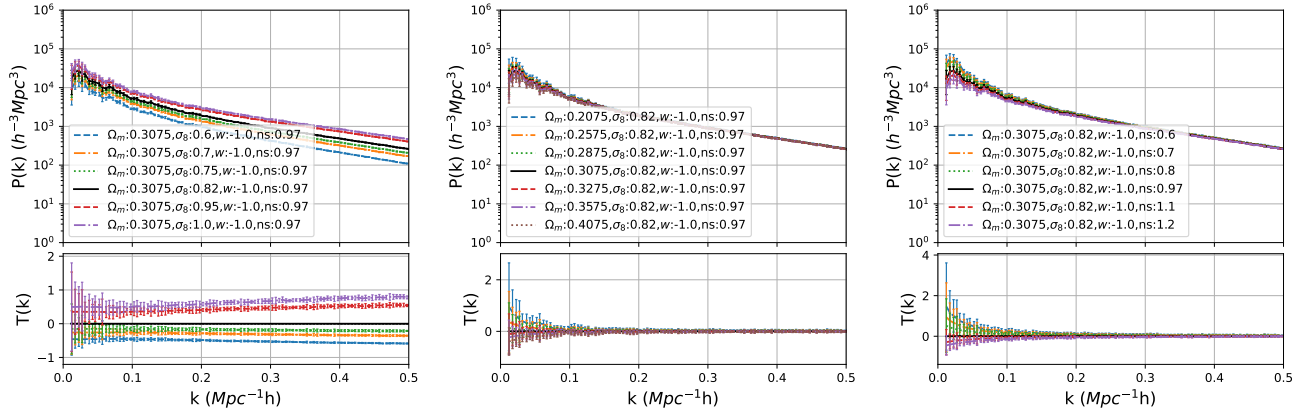


**Figure 28.** Using the initial matter fluctuation to explain the differences observed in the filament length distribution with respect to various cosmological parameters.

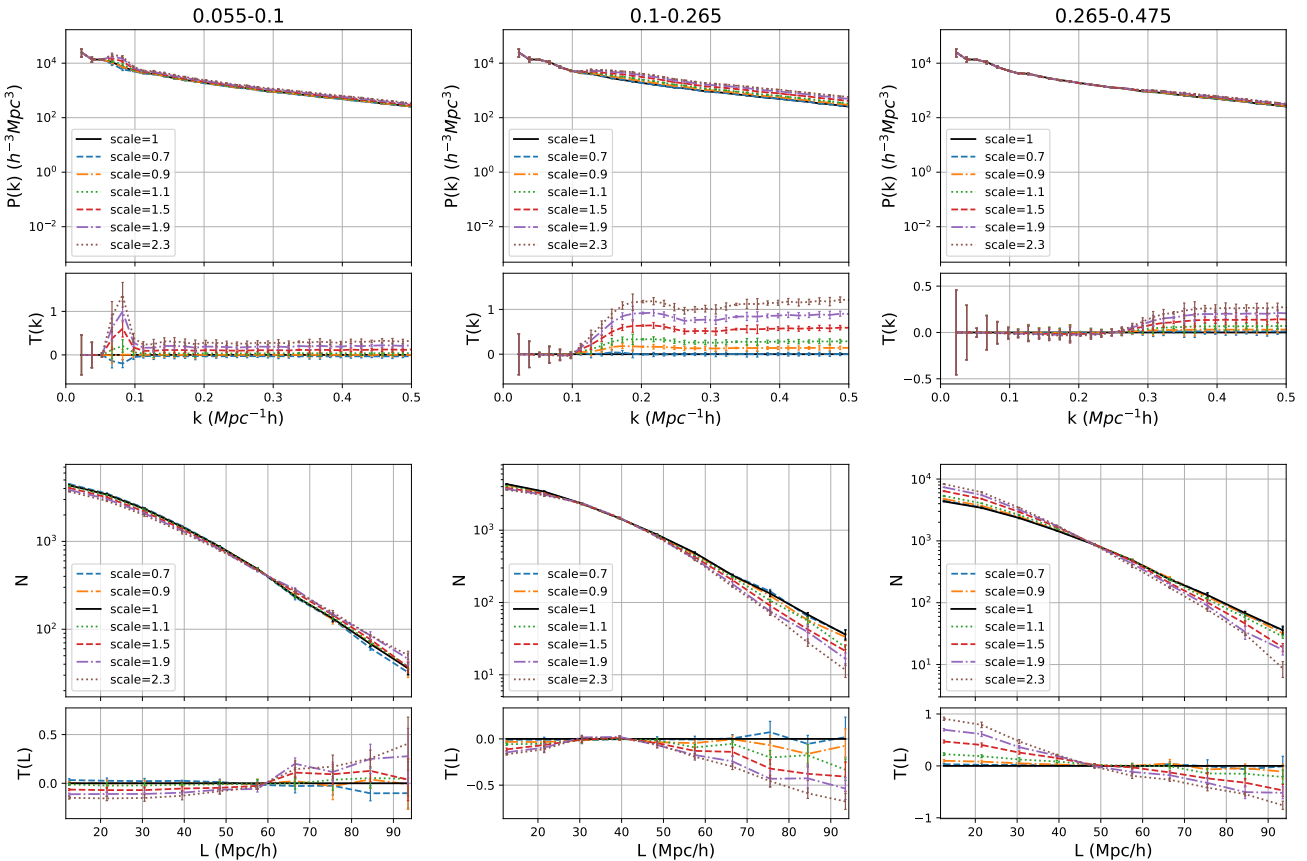


**Figure 29.** Characteristic length of filaments finding with dichotomy methods. The fluctuations at different scales  $k \in [0.055, 0.1, 0.265, 0.475]$  result in changes to both filament formation and the large-scale structure. The first row of our results displays the obtained power spectra, with each column representing a different scale modification. The second row exhibits the corresponding filament length distribution, which allows us to determine the characteristic length of filaments. We found that the filament characteristic length is approximately  $k \sim 0.265$ .

of cosmological parameters. The DisPerSE method, in particular, allows for the identification of all dark matter particles belonging to a filament. Utilizing these dark matter particles to measure the two-point correlation function or power spectrum can improve the signal-to-noise ratio and provide better constraints on cosmological parameters compared to using all particles for the measurement. The study of [Bonnaire et al. \(2022a,b\)](#) emphasizes the importance

of using multiple large-scale structural components to measure the power spectrum for better constraining cosmological parameters. However, [Bonnaire et al. \(2022a,b\)](#) employs the geometric Hessian-based method to identify filaments, while we use the topological DisPerSE method to investigate if different filament identification methods can lead to improved cosmological constraints. The power spectrum calculated for different cosmological parameters are shown

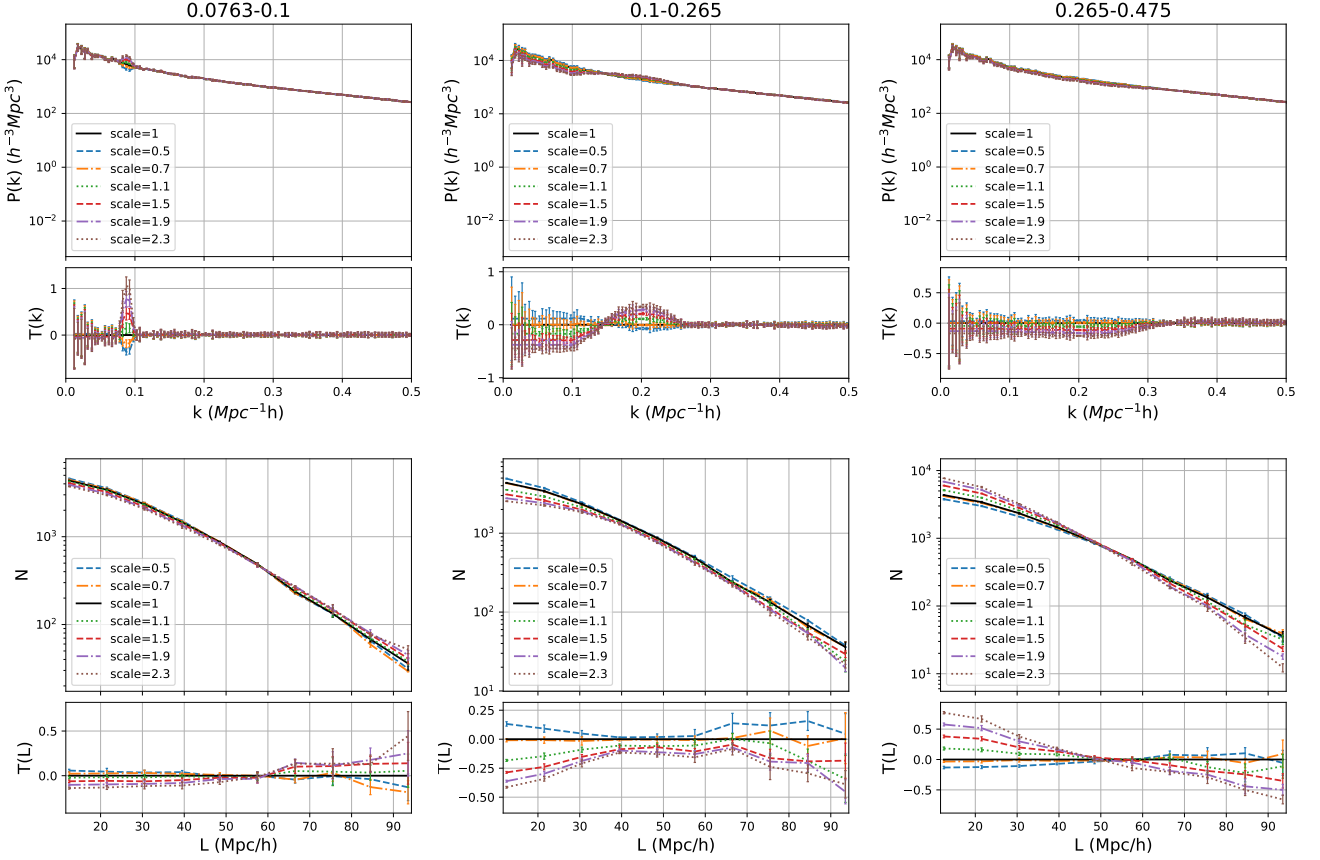


**Figure 30.** Similar to Fig. 29, but using normalized initial power spectra with the same  $\sigma_8$  value. This analysis enables us to investigate whether the characteristic length is dependent on  $\sigma_8$ .

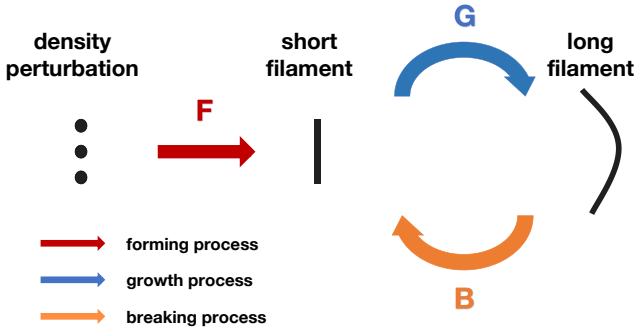


**Figure 31.** A toy model to depict the formation and transformation of short and long filaments. The (F) process corresponds to the filaments forming process caused by density perturbations, and (B) represents the breaking down process from long filaments to short filaments. In addition, (G) represents the growth process from short filaments to long filaments.

in Fig. 23 for dark matter particles and those inside filaments in Fig. 24. Here we can figure out that particles in filament shows a stronger clustering in filament than background particles which has also been investigated by previous studies (Xia et al. 2017; Paranjape et al. 2018; Yang et al. 2017). This strong clustering originated from the tidal field suggested an additional factors other than halo bias must be taken into account in linear tidal model which describes

the correspondence between halo shape and the local tidal field, as well as its environmental dependence. (Xia et al. 2017) Our results, presented in Fig. 25, show that using the disperse method to measure two-point correlation functions of filament particles found with this method can improve the signal-to-noise ratio for the cosmological parameter and provide better constraints on cosmology  $n_s$ , and nearly similar result for  $\Omega_m$ . To identify filament particles, we select all particles within a perpendicular distance of  $3Mpc/h$  of the filament central spine.

### 3.5 Initial condition

We have investigated the impact of cosmological initial conditions on filament formation and scrutinized the effect of fluctuations of different scales. In numerical simulations, the initial matter distribution is obtained by sampling the initial power spectrum, which means that changing the amplitude of a specific scale of the initial power spectrum can affect the magnitude of the fluctuation of that scale. To investigate this effect, we have selected four specific intervals ( $k \in [0.02, 0.1, 0.2, 0.3, 0.4]$ ) and added an artificial signal with different amplitudes to each interval, generating 40 modified power spectra in total. We employ a straightforward approach to adjust the power spectra. Following the selection of specific intervals, we calculate the mean value of the power spectrum within this interval. Subsequently, a variable *scale* is introduced to determine the location of the mean power spectrum value. This process is defined by the

following equations:

$$\begin{cases} P_{\text{mean}} = \frac{1}{2}(P_{\text{begin}} + P_{\text{end}}) \\ k_{\text{mean}} = \text{scale} \cdot (k_{\text{end}} - k_{\text{begin}}) + k_{\text{begin}} \end{cases} \quad (10)$$

Following this, a quadratic interpolation is applied to derive the complete modified power spectrum. As shown in Fig. 26 shows the initial power spectrum we generate in one of the intervals with different amplitudes. By passing these modified power spectra through our filament pipeline, we can obtain filament length functions and calculate nonlinear power spectra at  $z = 0$ . Fig. 27 shows that modifying the fluctuations of different scales in the initial power spectrum results in changes in the formation of filaments and the large-scale structure. The first row displays the power spectrum at  $z = 0$  obtained from passing the modified power spectra through our filament pipeline. The power spectra reflect the impact of the modified fluctuations of different scales on the large-scale structure. The second row exhibits the corresponding filament length distribution, revealing how the modifications affect filament formation. Increasing the amplitude of large-scale fluctuations (panels 1 and 2) leads to the formation of longer filaments while decreasing the total number of filaments. Conversely, increasing small-scale fluctuations (panels 3 and 4) has the opposite effect; it leads to shorter filaments and more filaments overall. This can be observed as an increase in power on a large scale, signifying the connection of more short filaments to form longer ones. Notably, at  $k \sim 2$ , a reversed correlation occurs in the filament length function. These findings provide insight into the impact of fluctuations of varying scales on the development of the cosmic web, indicating the possibility of an equilibrium point for the length of filaments on a characteristic scale where significant changes no longer occur. Our results also imply that large-scale changes cause short filaments to merge into longer ones, while small-scale changes prompt the collapse of smaller structures into clusters, truncating filaments as a result. This analysis may be utilized to understand the effect of the cosmological parameter  $n_s$  and  $\Omega_m$  on the filament length function considering the power spectrum of different  $n_s$  and  $\Omega_m$  in Fig. 28. For larger  $n_s$  and  $\Omega_m$ , the large scale of the power spectrum is larger causing the construction of long filaments.

In order to find the characteristic scale, we divide the  $k$  mode in log-scale and use dichotomy method to identify the scale showing up reversing, namely  $k \in [0.02, 1.0]$ . In Fig. 29, we find the characteristic scale to be around  $k \sim 0.265$ , showing that changes in matter fluctuations larger than this scale result in the formation of long filaments, whereas changes smaller than this scale have the opposite effect. We also check this without changing the value of  $\sigma_8$  in Fig. 30, showing that the characteristic scale still exists. This phenomenon is reasonable because increasing power on large scales results in a reduction of power on small scales when fixing  $\sigma_8$ , consequently leading to the decrease of small filaments. Additionally, the heightened power on larger scales also leads to the increase in longer filaments. Further exploration need to be done to understand the physical nature of the so-called filament characteristic scale.

## 4 CONCLUSION

The large-scale structure of the Universe contains a wealth of cosmological information, and as a member of the large-scale structure, the filament's definition and search method have been widely discussed in previous studies. At the same time, filaments have also been widely used in studies of galaxy formation. As a member of the large-scale structure, filaments actually contain a lot of cosmological information. Their physical and statistical quantities should

be regarded as cosmological probes and widely applied in cosmological studies. This study is innovative in its statistical analysis of length, which is the most direct, simple, and effective way to describe large-scale structure in filaments. We investigated the impact of three different cosmological parameters,  $\sigma_8$ ,  $\Omega_m$ , and  $n_s$ , on the filament length function. We found that the filament length function can serve as a relatively direct and effective cosmological probe. Although it is less sensitive than the halo mass function, it is easier to observe with reduced measurement error. We also explored the reasons for the differences in the filament length function in different cosmologies. We found that clustering tendencies and fluctuations at different scales have varying degrees of impact on filaments of different lengths. We found that larger  $\Omega_m$  leads to the formation of more clusters and hence the break-up of more filaments, while smaller  $\sigma_8$  make it harder to form filament structures.

We also studied the differences in the filament length function at different redshifts and defined a filament evolution function to track the formation and evolution of filaments under different cosmologies. We found that filament formation mainly undergoes three different stages, and different cosmologies may accelerate these stages. However, from redshift 3 to 2, filaments go through the first stage, where filaments of different lengths all form and grow. This conclusion holds true for different cosmologies. We also explored that  $\Omega_m$  has little effect on the low-redshift evolution of filament structure, mainly reflecting in long filaments.

Furthermore, we analyzed the constraints on cosmology from the filament power spectrum and the matter power spectrum, finding that different filament search methods have certain impacts on the cosmological constraints of filaments, but for some cosmological models, the filament power spectrum is better at constraining cosmology than the matter power spectrum, which verifies that extracting large-scale structure information to constrain cosmology may be an effective method.

Finally, we studied the impact of fluctuations at different scales on filament formation by analyzing the initial power spectrum fluctuations and found that large-scale fluctuations suppress the formation of short filaments while promoting the formation of long filaments, while small-scale fluctuations suppress the formation of long filaments. This conclusion can help to understand the impact of different cosmologies on the filament length function. Additionally, we found that there is a characteristic fluctuation scale in the filament length function, larger fluctuations than this scale will increase the formation of long filaments, and smaller fluctuations will reduce the formation of long filaments. Furthermore, this characteristic scale is still valid when fixed at  $\sigma_8$ , and further detailed discussions will be conducted in future work.

In summary, as a part of the large-scale structure of the Universe, filaments play an important role in cosmological research, and many statistical quantities can serve as cosmological probes applied to cosmological research.

## ACKNOWLEDGEMENTS

We acknowledge the support from the National Key Research and Development Program of China (No.2022YFA1602903), the NSFC (No. 11825303, 11861131006), the science research grants from the China Manned Space project with No. CMS-CSST-2021-A03, CMS-CSST-2021-B01, the Fundamental Research Funds for the Central Universities of China (226-2022-00216) and the start-up funding of Zhejiang University. RC acknowledges in part financial support from the start-up funding of Zhejiang University and Zhejiang provincial

top level research support program. We also acknowledge the cosmology simulation database (CSD) in the National Basic Science Data Center (NBSDC) and its funds the NBSDC-DB-10.

## DATA AVAILABILITY

The inclusion of a Data Availability Statement is a requirement for articles published in MNRAS. Data Availability Statements provide a standardised format for readers to understand the availability of data underlying the research results described in the article. The statement may refer to original data generated in the course of the study or to third-party data analysed in the article. The statement should describe and provide means of access, where possible, by linking to the data or providing the required accession numbers for the relevant databases or DOIs.

## REFERENCES

- Allys E., Marchand T., Cardoso J. F., Villaescusa-Navarro F., Ho S., Mallat S., 2020, *Phys. Rev. D*, **102**, 103506
- Alpaslan M., et al., 2014, *MNRAS*, **438**, 177
- Aragón-Calvo M. A., Jones B. J. T., van de Weygaert R., van der Hulst J. M., 2007, *A&A*, **474**, 315
- Aragón-Calvo M. A., van de Weygaert R., Jones B. J. T., 2010a, *MNRAS*, **408**, 2163
- Aragón-Calvo M. A., Platen E., van de Weygaert R., Szalay A. S., 2010b, *ApJ*, **723**, 364
- Bayer A. E., et al., 2021, *ApJ*, **919**, 24
- Bharadwaj S., Bhavsar S. P., Sheth J. V., 2004, *ApJ*, **606**, 25
- Bocquet S., et al., 2019, *ApJ*, **878**, 55
- Bond J. R., Kofman L., Pogosyan D., 1996, *Nature*, **380**, 603
- Bond N. A., Strauss M. A., Cen R., 2010, *MNRAS*, **409**, 156
- Bonnaire T., Aghanim N., Decelle A., Douspis M., 2020, *A&A*, **637**, A18
- Bonnaire T., Kuruvilla J., Aghanim N., Decelle A., 2022a, *arXiv e-prints*, p. [arXiv:2212.06838](https://arxiv.org/abs/2212.06838)
- Bonnaire T., Aghanim N., Kuruvilla J., Decelle A., 2022b, *A&A*, **661**, A146
- Cai Y.-C., Padilla N., Li B., 2015, *MNRAS*, **451**, 1036
- Cautun M., van de Weygaert R., Jones B. J. T., 2013, *MNRAS*, **429**, 1286
- Cautun M., van de Weygaert R., Jones B. J. T., Frenk C. S., 2014, *MNRAS*, **441**, 2923
- Cen R., Ostriker J. P., 2006, *ApJ*, **650**, 560
- Chen Y.-C., et al., 2017, *MNRAS*, **466**, 1880
- Cheng S., Ménard B., 2021, *arXiv e-prints*, p. [arXiv:2112.01288](https://arxiv.org/abs/2112.01288)
- Cheng S., Ting Y.-S., Ménard B., Bruna J., 2020, *MNRAS*, **499**, 5902
- Choi E., Bond N. A., Strauss M. A., Coil A. L., Davis M., Willmer C. N. A., 2010, *MNRAS*, **406**, 320
- Colless M., et al., 2003, *arXiv e-prints*, pp astro-ph/0306581
- Costanzi M., et al., 2019, *MNRAS*, **488**, 4779
- Costanzi M., et al., 2021, *Phys. Rev. D*, **103**, 043522
- DESI Collaboration et al., 2016, *arXiv e-prints*, p. [arXiv:1611.00036](https://arxiv.org/abs/1611.00036)
- Driver S. P., et al., 2011, *MNRAS*, **413**, 971
- Eickenberg M., et al., 2022, *arXiv e-prints*, p. [arXiv:2204.07646](https://arxiv.org/abs/2204.07646)
- Falck B. L., Neyrinck M. C., Szalay A. S., 2012, *ApJ*, **754**, 126
- Fang F., Forero-Romero J., Rossi G., Li X.-D., Feng L.-L., 2019, *MNRAS*, **485**, 5276
- Galárraga-Espinosa D., Aghanim N., Langer M., Gouin C., Malavasi N., 2020, *A&A*, **641**, A173
- Gheller C., Vazza F., 2019, *MNRAS*, **486**, 981
- González R. E., Padilla N. D., 2010, *MNRAS*, **407**, 1449
- Gualdi D., Gil-Marín H., Verde L., 2021, *J. Cosmology Astropart. Phys.*, **2021**, 008
- Gunn J. E., et al., 2006, *AJ*, **131**, 2332
- Hahn C., Villaescusa-Navarro F., 2021, *J. Cosmology Astropart. Phys.*, **2021**, 029
- Hahn C., Villaescusa-Navarro F., Castorina E., Scoccimarro R., 2020, *J. Cosmology Astropart. Phys.*, **2020**, 040
- Hamaus N., Sutter P. M., Lavaux G., Wandelt B. D., 2015, *J. Cosmology Astropart. Phys.*, **2015**, 036
- Hamaus N., Pisani A., Sutter P. M., Lavaux G., Escoffier S., Wandelt B. D., Weller J., 2016, *Phys. Rev. Lett.*, **117**, 091302
- Hamaus N., Cousinou M.-C., Pisani A., Aubert M., Escoffier S., Weller J., 2017, *J. Cosmology Astropart. Phys.*, **2017**, 014
- Hasselfield M., et al., 2013, *J. Cosmology Astropart. Phys.*, **2013**, 008
- Kraljic K., et al., 2018, *MNRAS*, **474**, 547
- Kraljic K., et al., 2019, *MNRAS*, **483**, 3227
- Kreisch C. D., Pisani A., Villaescusa-Navarro F., Spergel D. N., Wandelt B. D., Hamaus N., Bayer A. E., 2022, *ApJ*, **935**, 100
- Kuruvilla J., 2022, *A&A*, **660**, A113
- Kuruvilla J., Aghanim N., 2021, *A&A*, **653**, A130
- Kuutma T., Tamm A., Tempel E., 2017, *A&A*, **600**, L6
- Laigle C., et al., 2018, *MNRAS*, **474**, 5437
- Landy S. D., Szalay A. S., 1993, *ApJ*, **412**, 64
- Laureijs R., et al., 2011, *arXiv e-prints*, p. [arXiv:1110.3193](https://arxiv.org/abs/1110.3193)
- Li B., Zhao G.-B., Koyama K., 2012, *MNRAS*, **421**, 3481
- Li X.-D., Park C., Forero-Romero J. E., Kim J., 2014, *ApJ*, **796**, 137
- Li X.-D., Park C., Sabiu C. G., Kim J., 2015, *MNRAS*, **450**, 807
- Li X.-D., Park C., Sabiu C. G., Park H., Weinberg D. H., Schneider D. P., Kim J., Hong S. E., 2016, *ApJ*, **832**, 103
- Li X.-D., et al., 2018, *ApJ*, **856**, 88
- Libeskind N. I., et al., 2018, *MNRAS*, **473**, 1195
- Luo X., Wu Z., Li M., Li Z., Sabiu C. G., Li X.-D., 2019, *ApJ*, **887**, 125
- Malavasi N., et al., 2017, *MNRAS*, **465**, 3817
- Mantz A., Allen S. W., Rapetti D., Ebeling H., 2010, *MNRAS*, **406**, 1759
- Martizzi D., et al., 2019, *MNRAS*, **486**, 3766
- Massara E., Villaescusa-Navarro F., Ho S., Dalal N., Spergel D. N., 2021, *Phys. Rev. Lett.*, **126**, 011301
- Massara E., et al., 2022, *arXiv e-prints*, p. [arXiv:2206.01709](https://arxiv.org/abs/2206.01709)
- Mueller E.-M., de Bernardis F., Bean R., Niemack M. D., 2015, *ApJ*, **808**, 47
- Paillas E., Cai Y.-C., Padilla N., Sánchez A. G., 2021, *MNRAS*, **505**, 5731
- Paillas E., et al., 2023, *MNRAS*,
- Pandey B., Kulkarni G., Bharadwaj S., Souradeep T., 2011, *MNRAS*, **411**, 332
- Paranjape A., Hahn O., Sheth R. K., 2018, *MNRAS*, **476**, 3631
- Philcox O. H. E., Aviles A., Massara E., 2021, *J. Cosmology Astropart. Phys.*, **2021**, 038
- Philcox O. H. E., Ivanov M. M., Cabass G., Simonović M., Zaldarriaga M., Nishimichi T., 2022, *Phys. Rev. D*, **106**, 043530
- Pimblet K. A., Drinkwater M. J., Hawkrigg M. C., 2004, *MNRAS*, **354**, L61
- Pisani A., Sutter P. M., Hamaus N., Alizadeh E., Biswas R., Wandelt B. D., Hirata C. M., 2015, *Phys. Rev. D*, **92**, 083531
- Planck Collaboration et al., 2016, *A&A*, **594**, A24
- Pogosyan D., Pichon C., Gay C., Prunet S., Cardoso J. F., Sousbie T., Colombi S., 2009, *MNRAS*, **396**, 635
- Scodreggio M., et al., 2018, *A&A*, **609**, A84
- Smith A. G., Hopkins A. M., Hunstead R. W., Pimblet K. A., 2012, *MNRAS*, **422**, 25
- Sousbie T., 2011, *MNRAS*, **414**, 350
- Spergel D., et al., 2015, *arXiv e-prints*, p. [arXiv:1503.03757](https://arxiv.org/abs/1503.03757)
- Tanimura H., et al., 2019, *MNRAS*, **483**, 223
- Tempel E., Stoica R. S., Martínez V. J., Liivamägi L. J., Castellan G., Saar E., 2014, *MNRAS*, **438**, 3465
- Tempel E., Stoica R. S., Kipper R., Saar E., 2016, *Astronomy and Computing*, **16**, 17
- Uhlemann C., Friedrich O., Villaescusa-Navarro F., Banerjee A., Codis S., 2020, *MNRAS*, **495**, 4006
- Valogiannis G., Dvorkin C., 2022a, *Phys. Rev. D*, **105**, 103534
- Valogiannis G., Dvorkin C., 2022b, *Phys. Rev. D*, **106**, 103509
- Verza G., Pisani A., Carbone C., Hamaus N., Guzzo L., 2019, *J. Cosmology Astropart. Phys.*, **2019**, 040
- Vikhlinin A., et al., 2009, *ApJ*, **692**, 1060
- Wang Y., He P., 2022, *ApJ*, **934**, 112
- Wang Y., Yang H.-Y., He P., 2022, *ApJ*, **934**, 77

- Wilding G., Nevenzeel K., van de Weygaert R., Vegter G., Pranav P., Jones B. J. T., Efstathiou K., Feldbrugge J., 2021, *MNRAS*, **507**, 2968
- Woodfinden A., Nadathur S., Percival W. J., Radinovic S., Massara E., Winther H. A., 2022, *MNRAS*, **516**, 4307
- Xia Q., Kang X., Wang P., Luo Y., Yang X., Jing Y., Wang H., Mo H., 2017, *ApJ*, **848**, 22
- Xiao X., et al., 2022, *MNRAS*, **513**, 595
- Yang X., Mo H. J., van den Bosch F. C., Jing Y. P., 2005, *MNRAS*, **357**, 608
- Yang X., et al., 2017, *ApJ*, **848**, 60
- Yang Y., et al., 2020, *ApJ*, **900**, 6
- Zel'dovich Y. B., 1970, *A&A*, **5**, 84
- de Graaff A., Cai Y.-C., Heymans C., Peacock J. A., 2019, *A&A*, **624**, A48

## APPENDIX A: ROBUSTNESS

In Sec.2.1, several variable parameters in filament pipeline were identified, which are particle number  $N_p$  in numerical simulation, grid number of lattice points  $N_{grid}$  required for construction field from point cloud, and smoothing scale of field  $N_{smooth}$ . The effect of the first parameter is closely related to the observation, i.e. what effect the observed completeness of the galaxy has on the filament length statistics. In Fig. A2, we compare the effects of different particle numbers  $N_p$  in numerical simulations on filament length statistics. In a  $512(Mpc/h)^3$  box, the distribution of filament length larger than  $8Mpc/h$  with particle numbers of  $256^3$  and  $512^3$  are similar, but the simulation with a particle number of  $128^3$  is quite different. This means that when the completeness is greater than a certain threshold, it can describe the filament length distribution nearly the same as the complete samples.

Additionally, we discovered that the filament identified by DisPerSE is influenced to a certain degree by both the number of grid points, denoted as  $N_{grid}$ , and the smoothing scale of the field, denoted as  $N_{smooth}$ . We randomly choose a slice of  $z = 0$  density field generated from numerical simulation with a size of  $10 * 512 * 512(Mpc/h)^3$  and compare it with different smooth scale 1, 2,  $4Mpc/h$  in Fig. A4 and different grid point 128, 256, 512 in Fig. A5, from top to bottom on the left column and their corresponding filament found by DisPerSE on the right column. Specifically, we observed that increasing the number of grid points and decreasing the smoothing scale lead to an increased number of filaments being detected. The effect between the two is not exactly the same. The value of  $N_{grid}$  is predominantly limited by the accuracy of particle position observations. Coarse fields and smaller  $N_{grid}$  values result from imprecise observations, leading to the elimination of small-scale information and minor structural details. As a consequence, the detection of short filament structures and small void structures is compromised, resulting in longer filament connections. On the other hand, smoothing involves eliminating the random noise introduced by the lattice process from point cloud to field. While this reduces the detection of short filaments caused by noise, it also lengthens the filaments further. In Fig.A3, the left panel illustrates the impact of varying smooth scales  $N_{smooth}$  on filament length distribution, while the middle panel portrays the influence of different grid numbers  $N_{grid}$  on the same distribution. Finally, the right panel presents a comparison of the effects of smooth scales  $N_{smooth}$  and grid points  $N_{grid}$  on filament length distribution. Assuming that smooth scale  $N_{smooth}$  and grid number  $N_{grid}$  have the same effect on filament length distribution, we expected that after adding a fairly smooth scale, the black line of the middle graph in Fig. A3 would turn to the blue or yellow line. But as shown on the right panel, this is not the case. The effect of smooth scale  $N_{smooth}$  and grid number  $N_{grid}$  on filament length distribution is not exactly the same. A fairly smooth

scale will erase more short filament than grid number, i.e. smoothing are more likely to connected short filaments, resulting in more extended filament, while reducing the number of grid points will not only create void structures to extend filament but also generate more peaks to break some long filaments, resulting in fewer extended filaments than a smooth one. These can also be seen in Fig. A6, where we compare a slice of density field with mix of  $N_{grid}$  and  $N_{smooth}$ , i.e.  $N_{grid} = 512, N_{smooth} = 2$ ,  $N_{grid} = 256, N_{smooth} = 1$  and  $N_{grid} = 128, N_{smooth} = 0$  respectively from top to bottom.

As the focus of this paper is on the cosmological dependence of filament length distribution, it is important to ensure that our field structure is as realistic and accurate as possible in theory, in order to draw essential and physical conclusions and avoid the introduction of numerical noise. Therefore, we have used a 512 grid point, which guarantees the accuracy of our conclusions in theory and is perfectly adequate for the cosmological scale we are studying. Furthermore, we have also applied our analysis to a coarser grid to test whether the inaccuracy caused by observation errors in the observation will affect the application of our conclusion, i.e., whether the cosmological signal in filament length distribution is overwhelmed by observation errors. Additionally, to remove the effect of noise introduced by the lattice process, we have used a  $2Mpc/h$  smoothing scale. As shown in Fig.A4, this smoothing scale is appropriate.

The size of simulation box also has an effect on the analysis of filament length distribution. We tested the normalized filament length distribution for simulations with a box size of  $300(Mpc/h)^3$  and  $512(Mpc/h)^3$  in Figure A1, using 5 random seeds for each box size. Our analysis revealed that the variance resulting from the box size is negligible and does not impact our findings. In principle, the larger the box, the better it is for the analysis as a larger box means more filament samples and extended filaments. However, due to limited computing resources, we have chosen a  $512(Mpc/h)^3$  box which is enough for our study. Therefore, for most of this discussion, we choose a  $512(Mpc/h)^3$  box to find filament, with  $N_p = 256$ ,  $N_{grid} = 512$ , and  $N_{smooth} = 2Mpc/h$ . We believe that this selection ensures the effectiveness and accuracy of the analysis to the greatest extent while avoiding numerical noise.

This paper has been typeset from a  $\text{\LaTeX}$  file prepared by the author.

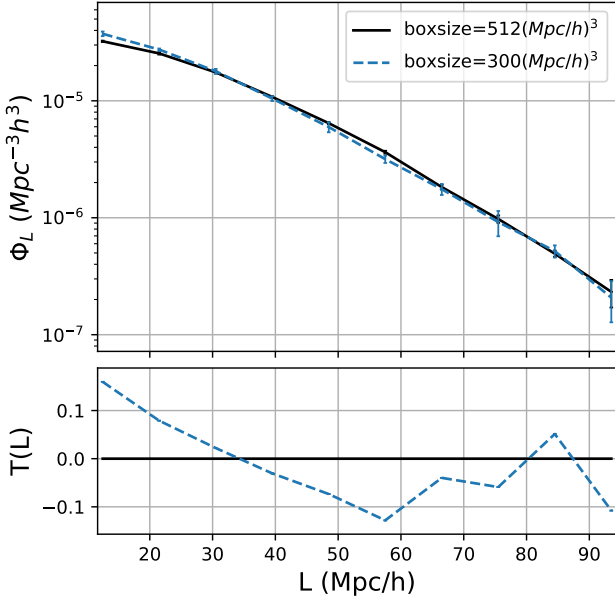


**Figure A1.** Robustness of simulation box size in filament pipeline. The filament length distributions obtained from simulations using box sizes of  $300(\text{Mpc}/h)^3$  and  $512(\text{Mpc}/h)^3$  are found to be quite similar with  $N_{\text{grid}} = 512$  and  $N_{\text{smooth}} = 2\text{Mpc}/h$ .

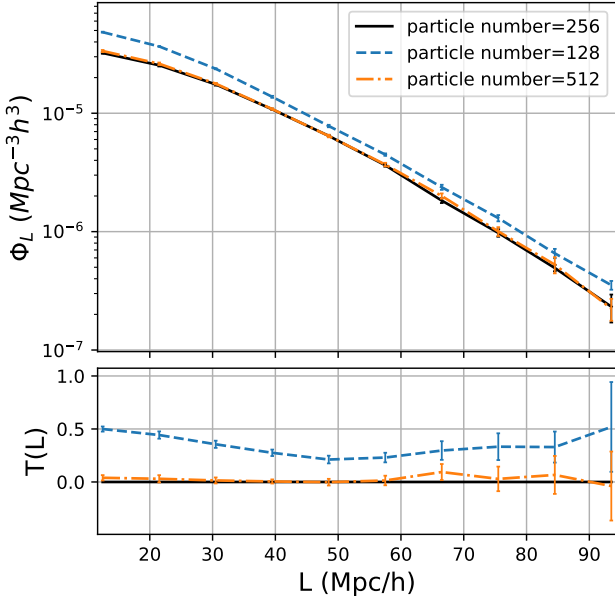


**Figure A2.** Robustness of the variable parameter  $N_p$  in filament pipeline. The filament length distributions of  $256^3$  and  $512^3$  particles used in numerical simulations are basically close to each other in a  $512^3(\text{Mpc}/h)^3$  simulation with  $N_{\text{grid}} = 512$  and  $N_{\text{smooth}} = 2\text{Mpc}/h$ , but a simulation with a number of  $128^3$  particles is somewhat different. This means that when the completeness is greater than a certain threshold, it can basically describe the filament length distribution nearly the same as the complete samples when choosing a certain  $N_{\text{grid}}$  and  $N_{\text{smooth}}$ .

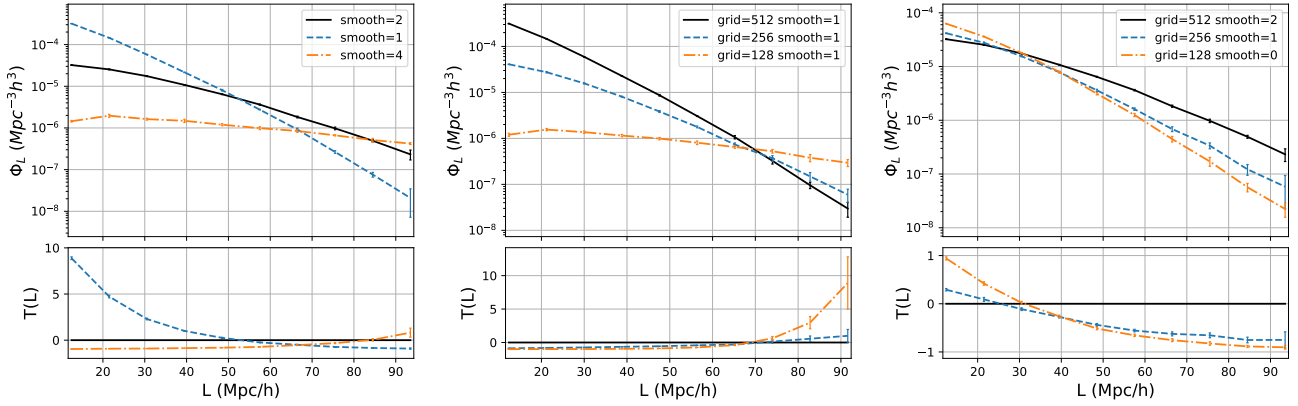


**Figure A3.** Robustness of the variable parameter  $N_{grid}$  and  $N_{smooth}$  in filament pipeline. The left panel illustrates the impact of varying smooth scales  $N_{smooth}$  on filament length distribution, while the middle panel portrays the influence of different grid numbers  $N_{grid}$  on the same distribution. Finally, the right panel presents a comparison of the effects of smooth scales  $N_{smooth}$  and grid points  $N_{grid}$  on filament length distribution.

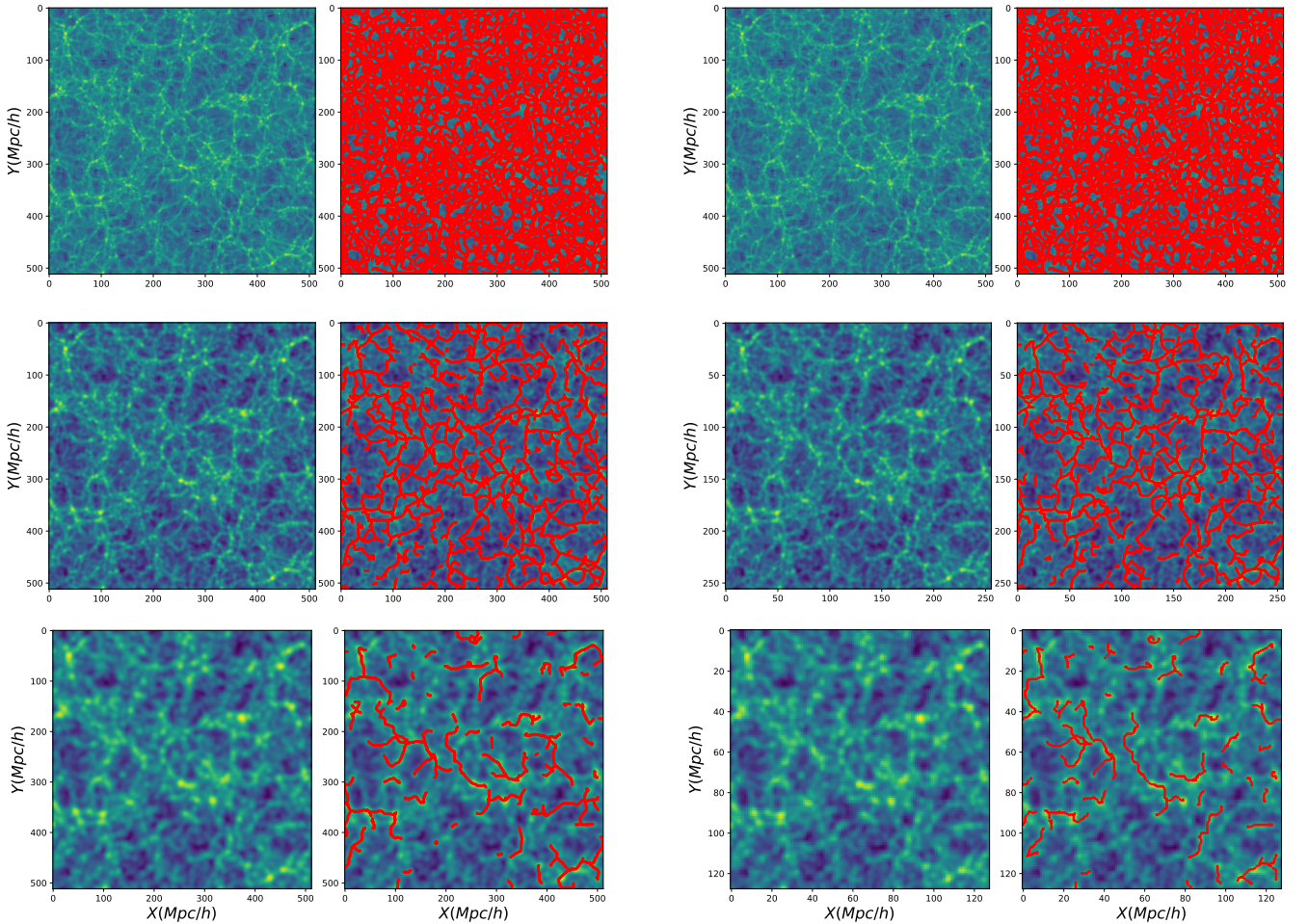


**Figure A4.** Visual comparison for different smooth scales in Planck15 cosmology. A slice of the density field with size of  $20 * 512 * 512 (Mpc/h)^3$  with  $N_{smooth} = 1, 2, 4 (Mpc/h)$  from top to bottom on the left panel and the filament found by DisPerSe with the corresponding smooth scales on the right panel.

**Figure A5.** Visual comparison for different lattice number in Planck15 cosmology. A slice of the density field with size of  $20 * 512 * 512 (Mpc/h)^3$  with  $N_{grid} = 512, 256, 128$  from top to bottom on the left panel and the filament found by DisPerSe with the corresponding lattice number on the right panel.

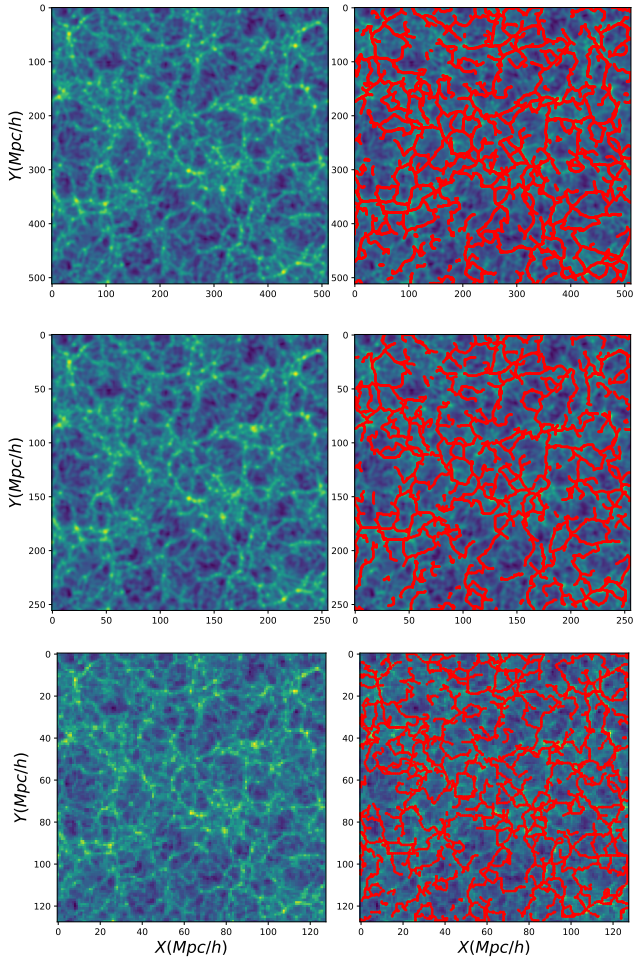


**Figure A6.** Visual comparison for mix of smooth scales  $N_{smooth}$  and lattice number  $N_{grid}$  in Planck15 cosmology. A slice of the density field with size of  $20 * 512 * 512 (Mpc/h)^3$  with  $N_{smooth} = 2, 1, 0 (Mpc/h)$  and  $N_{grid} = 512, 256, 128$  from top to bottom on the left panel and the filament found by DisPerSe on the right panel.